Wintertime Formaldehyde: Airborne Observations and Source Apportionment over the Eastern United States

Jaime R. Green[1], Marc N. Fiddler[1], Dorothy L. Fibiger[2,3,†], Erin E. McDuffie[2,3 †], Janine Aquino[4], Teresa Campos[4], Viral Shah[5], Lyatt Jaeglé[5] Joel A. Thornton[5], Joshua P. DiGangi[6], Glenn M. Wolfe[7,8] Solomon Bililign[1], Steven S. Brown[2,9]

[1] Department of Physics & Applied Sciences and Technology, North Carolina A&T State University, Greensboro NC, 27411
[2] NOAA Chemical Sciences Laboratory, Boulder, CO, 80305
[3] Cooperative Institute for Research in Environmental Sciences, University of Colorado, Boulder, CO, 80309
[4] National Center of Atmospheric Research, Boulder, CO, 80307
[5] University of Washington, Seattle, WA, 98195
[6]NASA Langley Research Center, Hampton VA, 23681
[7]Atmospheric Chemistry and Dynamics Lab, NASA Goddard Space Flight Center, Greenbelt, MD, 20771
[8]Joint Center for Earth Systems Technology, University of Maryland, Baltimore County, Baltimore, MD, 21228
[9]Department of Chemistry, University of Colorado, Boulder, CO 80309
†Current address California Air Resources Board, Sacramento, CA, USA

† Current address Department of Energy, Environmental, and Chemical Engineering, Washington University in St. Louis, St. Louis, MO, USA

Corresponding author: Solomon Bililign (bililignsol@gmail.com)

Key Points:

- Primary emissions dominate the wintertime HCHO budget in the northeastern US, though secondary production impacts HCHO formation downwind of urban areas.
- Observed HCHO/CO emissions ratios are 2.3 - 15 times greater than the regionally-integrated National Emission Inventory (NEI) 2017 database.
- Point source HCHO emissions may be underestimated by a factor of 17 – 23, depending on fuel type.

Abstract

Formaldehyde (HCHO) is generated from direct urban emission sources and secondary production from the photochemical reactions of urban smog. HCHO is linked to tropospheric ozone formation, and contributes to the photochemical reactions of other components of urban smog. In this study pollution plume intercepts during the Wintertime INvestigation of Transport, Emissions, and Reactivity (WINTER) campaign were used to investigate and characterize the formation of HCHO in relation to several anthropogenic tracers. Analysis of aircraft intercepts combined with detailed chemical box modeling downwind of several cities suggest that the most important contribution to observed HCHO was primary emission. A box model analysis of a single plume suggested that secondary sources contribute 21±10% of observed HCHO. Ratios of HCHO/CO observed in the northeast U.S., from Ohio to New York, ranging from 0.2-0.6%, are consistent with direct emissions combined with at most modest photochemical production. Analysis of the nocturnal boundary layer and residual layer from repeated vertical profiling over urban influenced areas indicate a direct HCHO emission flux of 1.3×10^{14} molecules cm^{-2} h^{-1}. In a case study in Atlanta, GA, nighttime HCHO exhibited a ratio to CO (0.6 – 1.8%) and was anti-correlated with O_3. Observations were consistent with mixing between direct HCHO emissions in urban air masses with those influenced by more rapid HCHO photochemical production. The HCHO/CO emissions ratios determined from the measured data are 2.3 - 15 times greater than the NEI 2017 emissions database. The largest observed HCHO/CO was 1.7 – 1.8%, located near co-generating power stations.

1. Introduction

Formaldehyde (HCHO) is a short-lived, ubiquitous compound with an atmospheric lifetime on the order of a few hours with respect to photolysis and reaction with OH. HCHO in the urban environment has been identified as a carcinogen in outdoor air, and is among the 187 hazardous air pollutants, whose emissions are regulated by the U.S. Environmental Protection Agency (EPA) [*EPA*, 2015; *Zhu et al.*, 2017].

HCHO in the lower atmosphere stems from both direct emissions and secondary chemical production. Natural primary emission sources of HCHO include direct emission from vegetation, the soil, biomass burning and decaying plant and animal matter. In remote and rural areas the primary emission of HCHO from natural sources accounts for 10 – 20% of the total HCHO [*Luecken et al.*, 2018; *Zhang et al.*, 2013]. The remainder is produced from chemical oxidation of methane (CH_4) and other biogenic and anthropogenic VOCs (AVOCs) [*de Blas et al.*, 2019; *Luecken et al.*, 2018; *Zhang et al.*, 2013]. When vegetation is active (spring – fall), isoprene is the main HCHO precursor throughout much of the continental U.S. with a contribution of 20 – 90% along the eastern coastal U.S. [*de Blas et al.*, 2019; *Kurosu et al.*, 2007; *X Li et al.*, 2013; *Marvin et al.*, 2017]. When vegetation is dormant (winter months), anthropogenic activities are the dominant source of HCHO [*J Bai et al.*, 2018; *de Blas et al.*, 2019].

Anthropogenic emissions of HCHO and its precursors can also contribute significantly to the HCHO budget, especially in large urban areas [*Czader et al.*, 2008; *Guven and Olaguer*, 2011; *Lin et al.*, 2012]. Anthropogenic use of natural gas, diesel fuel, gasoline, and solid fuels such as coal and wood contribute to anthropogenic volatile organic compound (AVOC) precursors of HCHO and direct emissions of HCHO [*Alzueta and Glarborg*, 2003; *Clairotte et al.*, 2013]. Other anthropogenic sources of HCHO and AVOCs include landfills and industrial

82 sites involved in the production of polymers, construction materials, wood products and wood
83 processing, solvents, and glues [*Liang et al.*, 2016; *Salem and Böhm*, 2013; *Yrieix et al.*, 2010].
84 HCHO is still used for some cleaning practices in the agricultural industry [*de Gouw et al.*,
85 2017b; *Doane and Sarenbo*, 2014; *White et al.*, 2018]. The magnitude of the contribution to
86 HCHO from industrial refining and oil and gas production remains unclear [*Koss et al.*, 2015;
87 *Pikelnaya et al.*, 2013].

88 Constraints on the anthropogenic contribution to HCHO are best obtained in the absence
89 of significant biogenic contribution, but research grade observations in the winter are
90 uncommon. *Zhu et al.* [2017] noted that existing EPA monitoring measurements from sites near
91 urban and rural areas may not accurately resolve the concentration of HCHO in the stratified
92 winter atmosphere. Other studies that utilize 3D atmospheric chemistry transport models, such as
93 Community Multiscale Air Quality (CMAQ) and other Air Quality Models (AQMs), cite that
94 underestimation in HCHO is related to the underestimation of VOCs or a failure to capture and
95 quantify VOC precursors of HCHO from anthropogenic activities [*Luecken et al.*, 2012; *Luecken*
96 *et al.*, 2018; *Warneke et al.*, 2007; *Zhu et al.*, 2017]. Furthermore, aircraft missions investigating
97 regional air quality in the lower atmosphere have most commonly been conducted in the summer
98 when photochemical secondary HCHO production is most active [*Parrish et al.*, 2009a; *Ryerson*
99 *et al.*, 2013; *Warneke et al.*, 2016].

100 The Wintertime INvestigation of Transport, Emissions, and Reactivity (WINTER)
101 mission was designed to understand the processes controlling atmospheric composition in the
102 wintertime boundary layer of the Eastern U.S. A recent analysis of these observations has
103 revealed that HCHO can be as much as 50% of the daily integrated radical source (*Haskins et al.*
104 [2019]). Furthermore, *Jaeglé et al.* [2018] found a bias of -46% in GEOS-Chem simulated

HCHO concentrations relative to WINTER observations at altitudes < 1 km. This bias was eliminated in the model by increasing direct HCHO emissions from residential wood combustion and mobile sources by a factor of 5. Justification for the adjustment factor is based on the studies by *Jobson and Huangfu* [2016] which suggested that wintertime cold start HCHO emissions are underestimated by a factor of 5 and the study by *VanderSchelden et al.* [2017], which found that residential wood combustion accounts for a higher percentage of HCHO compared to what was expected from the National Emissions Inventory (NEI) inventory. Underestimation of wintertime HCHO concentrations and VOC precursors in modeling studies that utilize EPA monitoring data have also been reported by *Zhu et al.* [2017] and *Luecken et al.* [2012]. Uncertainties in emission inventories are thus large and have important consequences for simulating air quality-relevant photochemistry.

Here, we present a detailed analysis based on WINTER observations to investigate anthropogenic sources of HCHO near urban areas and power plants in the Eastern U.S. We use several analysis tools to segregate primary emissions and secondary production of HCHO, including a linear combination model, a detailed chemical box model constrained by observations downwind of urban areas, observations of HCHO accumulation rates in the nocturnal boundary layer, and examination of enhancement ratios relative to carbon monoxide (CO). Results are compared to several emissions inventories, global model simulations results, and other historical data to provide insight and constrain uncertainties in the HCHO budget.

2. Field Study and Instruments

2.1 WINTER Campaign Flight Description

126 The WINTER campaign was a six-week field campaign conducted from February 1 to
127 March 15, 2015 on the National Science Foundation/National Center for Atmospheric Research
128 (NSF/NCAR) C-130. Flights were based at the Langley Campus in Hampton, VA. The
129 campaigns consisted of 13 research flights (RF). Figure 1 shows the locations of flights used for
130 this study. Research flights include a day flight (RF 02), two midday-into-night flights (RF 03
131 and RF 04), and two night flights (RF 07 and RF 10). These flights sampled a variety of potential
132 HCHO sources, including urban areas with motor vehicle activity. Several plumes with apparent
133 HCHO emissions from natural gas and diesel fuel co-generating power stations were sampled
134 and quantified.

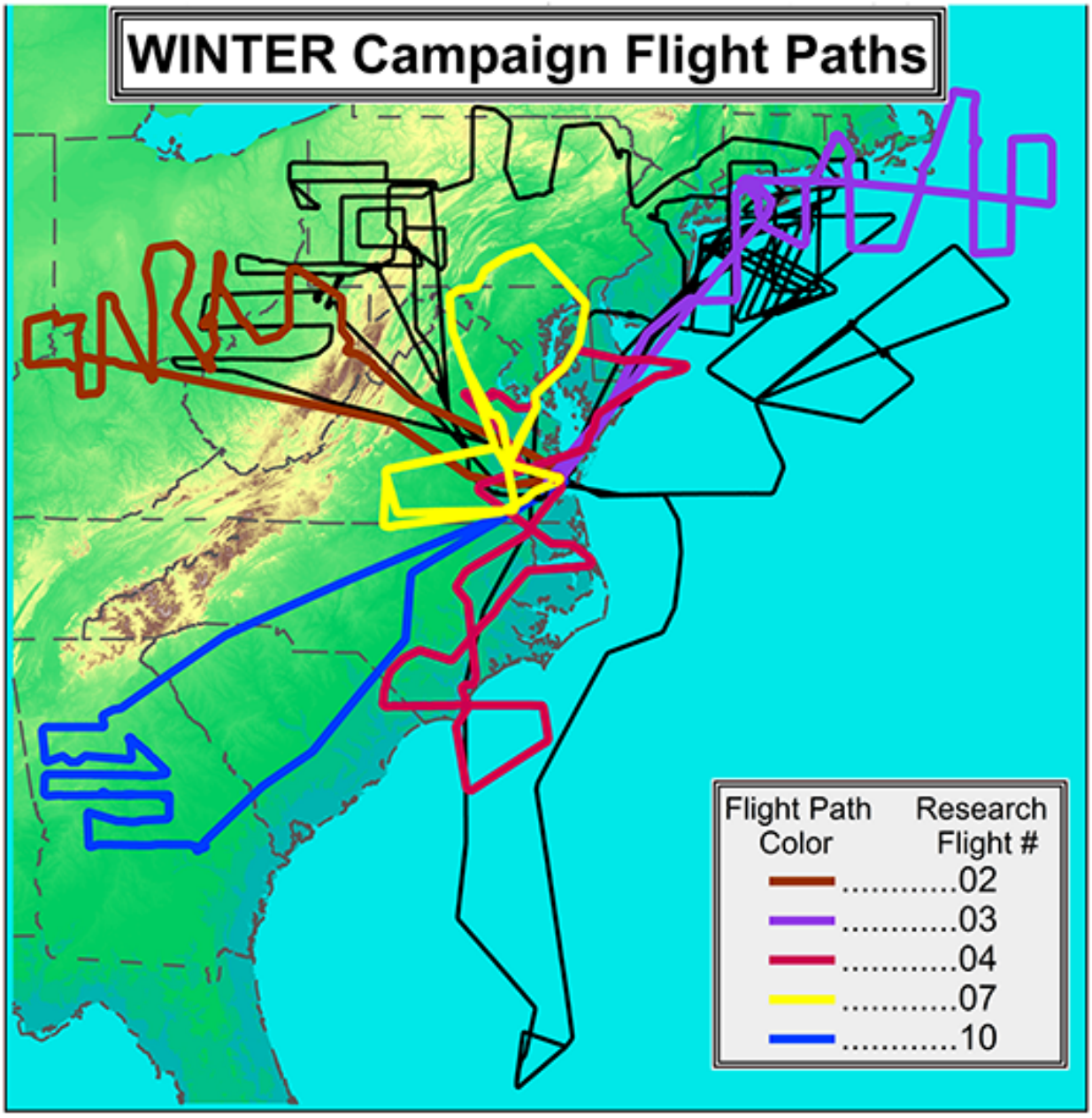


Figure 1: Flight tracks of the NSF C-130 aircraft during the 2015 WINTER campaign (black), with flight tracks used in this analysis identified by their corresponding color. Each flight occurred on the following dates in 2015: RF 02 on Feb. 06, RF 03 on Feb 07, RF 04 on Feb 11, RF 07 on Feb 24, RF 10 on Mar. 07.

135

136 2.2 Instrumentation

The NASA In Situ Airborne Formaldehyde (ISAF) instrument provided fast measurements of HCHO [*Cazorla et al.*, 2015] .ISAF has a nominal accuracy of 10% based on standard additions from a calibrated compressed-gas standard and a precision of ~30 pptv for an integration time of 1 second. On board instrumentation has been described in previous [*Fibiger et al.*, 2018; *Green et al.*, 2019]. *Sparks et al.* [2019] provided information about nitrogen species that were measured simultaneously with HCHO. The instruments used to measure each chemical species are described in Table 1 below.

Table 1

On Board Instruments Measuring, HCHO, O_3, Oxidized Nitrogen and Reactive Nitrogen Species

Instrument	Species	Uncertainty	Detection Limit	Reference
CRDS	O_3	3%	30 pptv	[*Brown et al.*, 2017; *Sparks et al.*, 2019; *Wild et al.*, 2014]
	NO	4%	35-140 pptv	
	NO_2	3%	25-114 pptv	
	NO_y	12%	50-380 pptv	
	N_2O_5	12%	1.3-4.4 pptv	
CL	O_3	0.5%	100 pptv	[*Sparks et al.*, 2019; *Weinheimer et al.*, 1994]
	NO	10%	30 pptv	
	NO_2	5%	70 pptv	
	NO_y	50%	100 pptv	
ISAF	HCHO	10%	30 pptv	[*Cazorla et al.*, 2015]
TD-LIF	NO_2	10%	20 pptv	[*Day et al.*, 2002; *Sparks et al.*, 2019]
Pulsed Fluorescence SO_2 Analyzer	SO_2		3% ± 0.5 ppbv	[*Green et al.*, 2019]

147 Oxidized nitrogen, NO_x (NO + NO_2), reactive nitrogen species NO_y (NO_x, NO_3, N_2O_5,
148 and other species), and O_3 were measured by a six-channel cavity ring-down spectrometer
149 (CRDS) [*Brown et al.*, 2017; *Wild et al.*, 2014]. A thermal dissociation laser induced
150 fluorescence (TD-LIF) instrument [*Day et al.*, 2002; *Sparks et al.*, 2019] measured NO_2 and
151 speciated reactive nitrogen, including alkyl and peroxy nitrates and HNO_3. A chemiluminescence
152 instrument (CL) also provided data for O_3, NO and NO_y [*Sparks et al.*, 2019; *Weinheimer et al.*,
153 1994]. A modified, rack mounted TECO Model 43C Pulsed Fluorescence SO_2 Analyzer
154 provided SO_2 gas measurements as described in *Green et al.* [2019]. Other measurements not
155 listed in Table 1 include the measurement of the actinic flux and photochemical rates of various
156 photochemical processes by the HIAPER Atmospheric Radiation Package (HARP) [*Laursen et*
157 *al.*, 2006], the measurement of CO_2 CH_4 using the Picarro CRDS, the measurement of CO using
158 commercial Aero-Laser AL-5002 VUV resonance fluorescence instrument [*Salmon et al.*, 2018;
159 *Yuan et al.*, 2015], and the measurement of volatile organic compounds by the TOGA instrument
160 [*Apel et al.*, 2015].

161 2.3 Pollution Plume Identification, Tracking and Analysis

162 Enhancements of HCHO relative to other pollutants were determined for plumes
163 intercepted aloft from both point sources (i.e., electric power generating stations) and urban
164 areas. Power station plumes were identified using the molar ratio of SO_2/NO_y for coal fired
165 power stations, and SO_2/NO_y, CO_2/NO_y, and CO/NO_y for co-generating power stations using a
166 combination of natural gas, bio-diesel, wood, coal and other fuels. These molar ratios were
167 determined from orthogonal distance regression (ODR) fits to plots of SO_2 versus NO_y, SO_2
168 versus CO, and CO_2 versus NO_y. SO_2/NO_y ratios were compared to the ratios of the
169 corresponding emissions of SO_2 and NO_x provided by the Environmental Protection Agency

(EPA) continuous emission monitoring (CEMS) database to identify plumes from coal fired power stations, with CO_2/NO_y used to identify co-generating stations. Emissions ratios calculated using the aggregate data from the NEI database from 2014 and 2017 in the form of yearly averages were also used for comparison, since HCHO data was not available in the CEMS database. Additionally, CO/NO_y was used to separate urban plumes, where urban air masses typically have a CO/NO_y ratio between 4 – 10, and power stations using diesel fuels have a CO/NO_y ratio greater than 20 [*Hassler et al.*, 2016; *C Li et al.*, 2010; *Parrish et al.*, 2009b]. Techniques for curve fitting, plume aging and tracking analysis, and the use of chemical ratios to differentiate urban from power station plumes are described in earlier work *[Green et al., 2019]*.

Hybrid Single-Particle Lagrangian Integrated Trajectory (HYSPLIT) back trajectory analysis, using the NAMS Hybrid sigma-pressure archived data set, was performed from a given plume intercept to 8 h prior to the intercept time to trace the point of origin back to a specific power station as described in *Green et al.* [2019]. HYSPLIT was used in combination with the wind field measurements taken by aircraft instrumentation to confirm the path and the approximate time carried aloft.

In addition to the techniques previously described, a linear model was applied for HCHO source apportionment using several chemical tracers: CO, CH_4, SO_2, and NO_x. The technique is described by *Rawlings et al.* [2001] and used by *Friedfeld et al.* [2002] and *Garcia et al.* [2006]. The multi-variable linear regression model assumes that HCHO variability can be described as a linear combination of variability in other correlated observations. The linear model is described by Equation 1 [*Garcia et al.*, 2006; *Rawlings et al.*, 2001].

(1) $$[Y] = b_0 + b_1[X_1] + b_2[X_2] + b_3[X_3] + \cdots + b_m[X_m]$$

Where Y and $X_1 \ldots X_m$ are matrices of dimension n × 1, and where n is the number of data points for each chemical tracer used. By definition [Y] represents the total [HCHO], where the dataset of [HCHO] input as an n × 1 matrix and the concentration of each chemical tracer species is represented by $[X_1]$, $[X_2]$, $[X_3]$, etc. The coefficients b_1 pertains to [CO] (as $[X_1]$), b_2 for background subtracted $[CH_4]$ (as $[X_2]$), etc. Using equation 1, these coefficients are solved for each tracer species data set that was used for a given linear model, as described in Section 3.1.1. The solution for these coefficients is used to determine the percent correlation of a chemical species X, in relation to [HCHO] input into Y by using Equation 2 [*Garcia et al.*, 2006]. The percent correlated to [HCHO] in the multivariable linear fit for the chemical species represented in the numerator in equation 2. The r^2 value is related to the percent variability in HCHO that can be attributed to changes in these species. Before each chemical species was used in the linear model, it was correlated to HCHO using ODR fitting to justify their use. Species that were individually correlated with HCHO were then used in the linear model. Each coefficient in the set predicts the association with each chemical tracer using Equation 2. The resulting data ranges, from the ODR correlation, were then used in the linear model to find the coefficients for the equation similar in form to Equation 1. These coefficients then can be used to determine the percent covariance of a chemical species to Y by using Equation 2 [*Garcia et al.*, 2006].

(2) $$\%\ covariance = \frac{\sum(b_1 \times [X_1])}{\sum(b_1 \times [X_1]) + \sum(b_2 \times [X_2]) + \sum(b_3 \times [X_3]) + \cdots \sum(b_n \times [X_n])}$$

Figure 2 provides a time series plot of observed HCHO, CO, CH_4, and SO_2, that is representative of the urban plumes inputted into the model. We anticipate that equation (2)

would only be valid during winter when primary HCHO associated with co-emission of other pollutants would be the dominant source. Secondary HCHO and, to a lesser extent, CO, would degrade the validity of this approach in summer. The concentrations for CO and CH_4 in the time series plot are the amounts above the background levels of 122 ppbv for CO and 1896 ppbv for CH_4, with the background level of each chemical species defined as the concentration measured in the absence of urban and power station pollution plumes. The resulting stacked plot at the bottom in Figure 2 only illustrates the amount [HCHO] that is attributed to the chemical tracers input into the model along with the portion [HCHO] attributed to the background concentration of HCHO or HCHO production from unaccounted sources of a chemical species, and is labeled B_0. The black line is the time series of HCHO ppbv measured over the intercepted plume as shown in the top of Figure 2. Portions of the data set where there was a gap in the recorded data of one or more of the chemical species were excluded from the linear model. The area under the black line is separated into regions that represent the percentages of each co-emitted compound attributed to the production of HCHO with a r^2 value of 0.67.

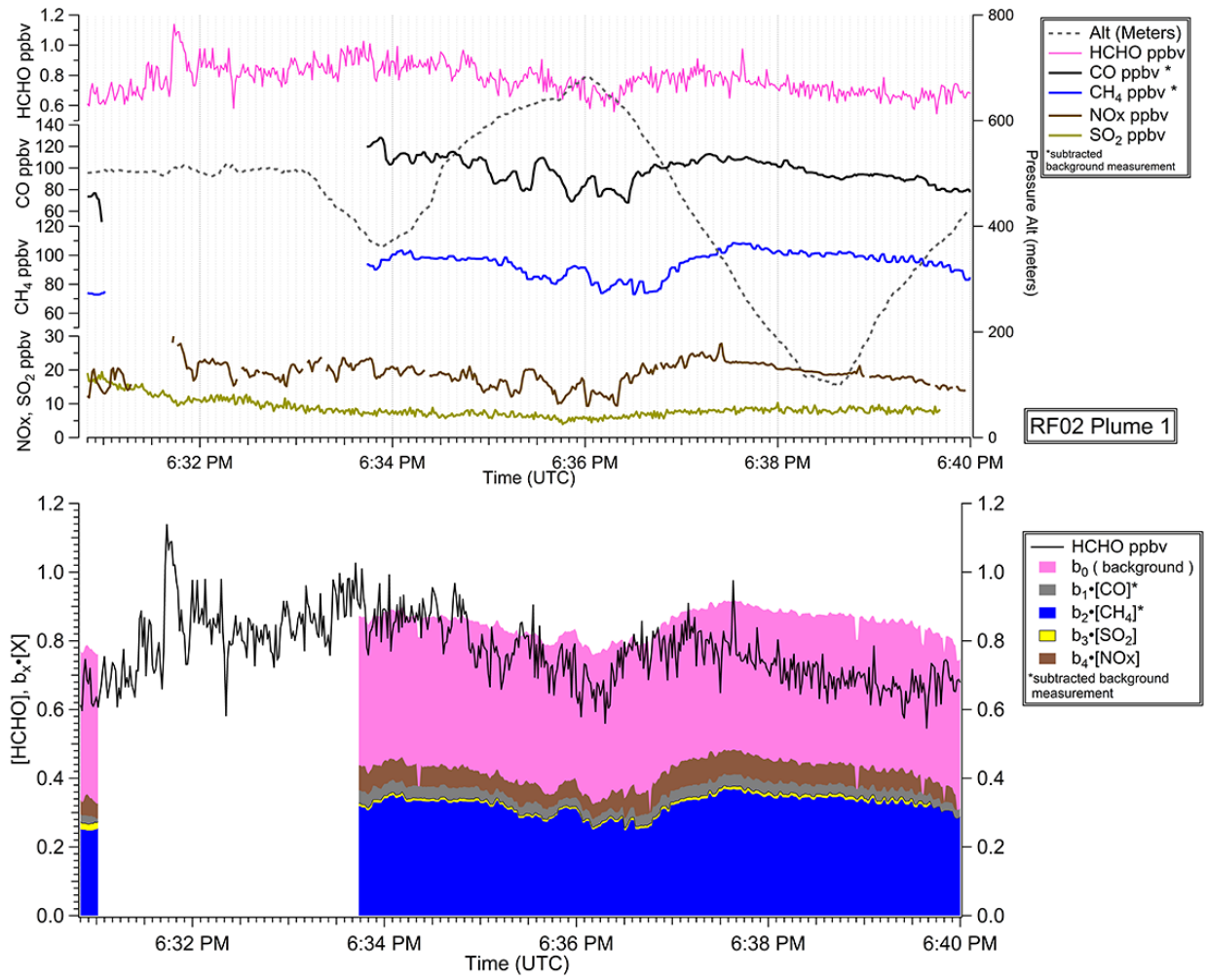


Figure 2: Figure 2: (Top) The time series plot uses data from RF02, plume 1, (see Figure 4) plotting in a stacked plot the amount of HCHO attributed by the specific chemical tracer marked with the colors in the legend. (Bottom) The time series plot of each of the chemical tracers inputted into equation 1 (CO, CH_4, SO_2, NOx) multiplied by the coefficients,b_1 …b_4, and b_0 taken as the average background concentration of HCHO as determined by the linear fit. Since the background concentration does not add to the total concentration of the plume, the percent correlation will be effectively zero when used in equation 2..

226

3. Results and Discussion

3.1 Daytime urban emissions and sources

The examination of daytime emissions of HCHO from the urban environment during the winter focuses on data obtained from flights RF02 and RF03. Figure 3 shows an example of plume 1 from RF03 (see Figure 7 for the map of RF 03). Figure 3 also is an example of the observations seen during RF02 and RF03, with the ratio of NO_x/NO_y equal to unity to within the uncertainty of the fit, giving evidence that very little photochemical oxidation of NO_x had occurred. The CO/NO_x ratio of 5.92 is consistent with analysis of urban emissions from major cities in the U.S. [*Bai et al.*, 2017; *Hassler et al.*, 2016]. We can also compare the value for HCHO/CO of 0.59% to the expected mixing ratio enhancements from primary emissions of HCHO and CO from the on-road vehicle fleet. *Parrish et al.* [2012] report an HCHO/CO ratio of 0.3%, while *Rappenglück et al*. [2010] report a ratio of 0.6% based on summertime observations. This comparison indicates that the ratio of 0.6%, is an upper limit to the direct emission of HCHO given that there is likely some contribution of photochemical / secondary production. In the absence of strong photochemistry, as seen in the winter, a lower limit for HCHO/CO ratio of 0.2% has been observed in urban plumes. The value is just slightly higher than the lowest value of 0.17% found during the summer morning peak traffic periods. The chemical box model analysis below provides a more quantitative estimate of the secondary contribution to observed HCHO.

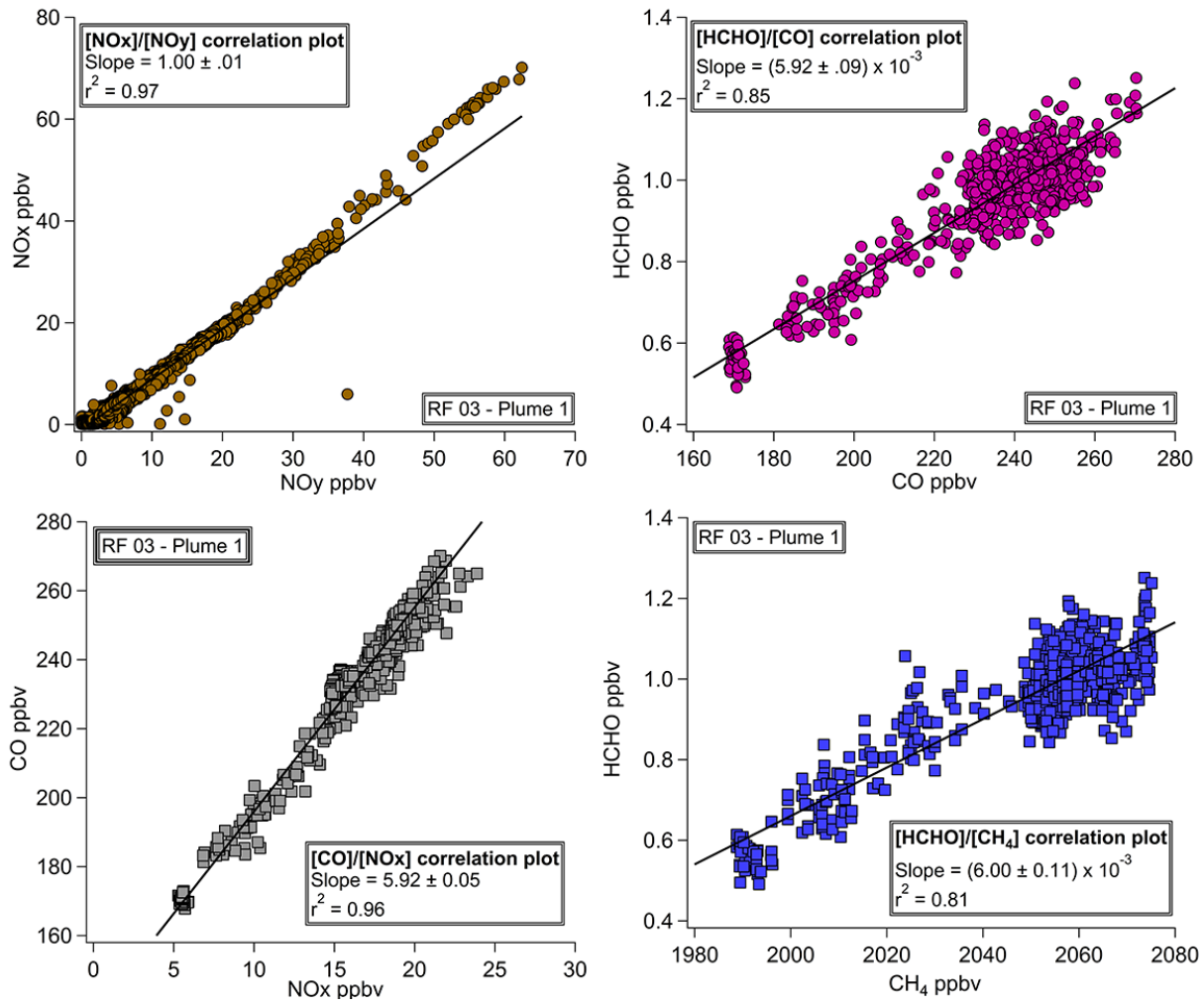


Figure 3: Examples of correlation plots, shown for RF 03, plume 1. Slopes and their errors (1σ) are listed in the legend along with their r^2 values.

For the urban areas investigated in RF02 and RF03, transport times calculated with observed winds agreeing to within 1 - 2 hrs with the HYSPLIT trajectories passing through the urban centers. HYSPLIT was used to estimate transport times for urban plumes 1 - 4 and 7, that share the same path of transport as indicated by the circles and wind barbs, and originate from Cincinnati, Ohio and pass over the urban area of Columbus, Ohio.

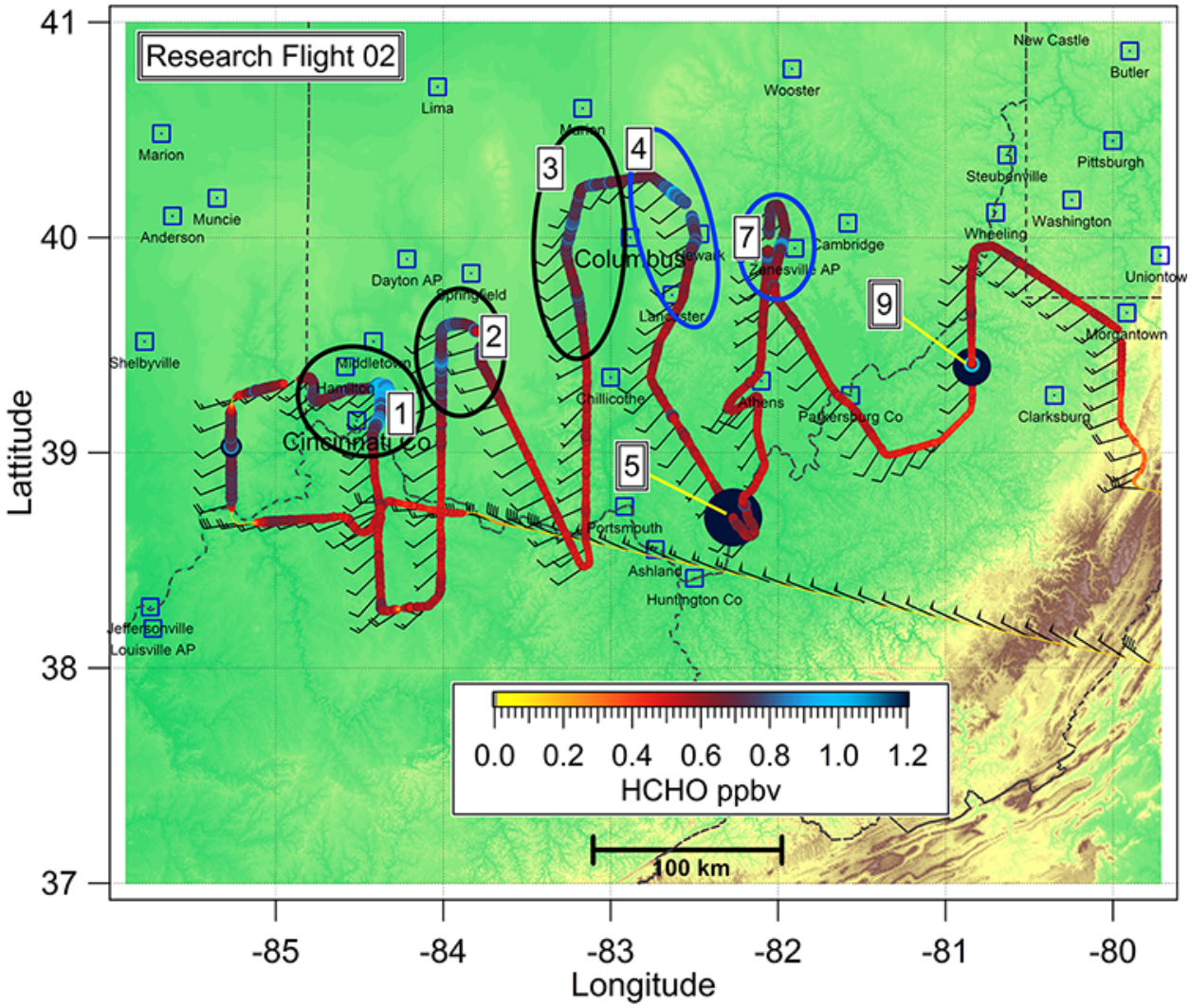


Figure 4: Flight track of the C-130 during Research Flight 02 (RF 02) on February 06, 2015. Open squares indicate urban areas. Background shading indicates terrain elevation. Each urban plume is identified by the regions enclosed in colored circles. The color of the circle indicates plumes that were attributed to the same source. The mixing ratio of HCHO along the flight path is indicated by the color scale and size of the marker, and measurements for points 5 (peak [HCHO] of 3.4 ppbv) and 9 (peak [HCHO] of 2.2 ppbv) are off the given scale.

252

253 3.1.1 Analysis of Urban Plumes over the Columbus and Cincinnati Urban Areas

254 Scatter plots of NO_x vs NO_y for urban plumes that were measured near cities in RF02
255 exhibited strong correlation ($r^2 > 0.95$) with ratios of NO_x/NO_y of 0.99, decreasing to 0.94 for
256 urban plumes that were carried aloft to 240 km downwind from the city center of Cincinnati,

Ohio. In general, the plumes belonging to the Cincinnati and Columbus, Ohio metropolitan areas were encountered at nearly the same altitude and correspond to CO concentrations in the range of 180 – 240 ppbv. The ratios of HCHO/CO in RF02 ranged between 0.26% to 0.50% and HCHO and CO were moderately correlated. Linear fits of HCHO to CO and other tracers give $r^2 > 0.44$ for HCHO to CO, $r^2 > 0.49$ for HCHO to NO_x and NO_y, $r^2 > 0.40$ for HCHO to CH_4, and $r^2 > 0.30$ for HCHO to SO_2. CO had very good correlations to methane with $r^2 > 0.89$, CO to NO_x and CO to NO_y , $r^2 > 0.95$ for both with NO_x/NO_y ratios close to 1.

Multiple linear regression analysis was applied to determine the percentage of HCHO that is connected to the presence of each of the tracers, or co-emitted compounds: CO, CH_4, SO_2, and NO_x. A correlation plot of the sum of PNs (peroxynitrates) from the TD-LIF instrument [*Day et al.*, 2002] is a test of possible secondary HCHO production. The correlation was poor, with an $r^2 < 0.12$ for plumes 1 – 4 and 7 in RF02. The low correlation of HCHO with reported PNs and a NO_x/NO_y ratios close to 1 is consistent with slow photochemistry cited by Sparks et al. [2019]. The results from the linear model, shown in Figure 5, have an $r^2 > 0.67$ for the multivariate fit for all four tracers in plume 1 over Cincinnati, and an $r^2 > 0.60$ for plume 4 over Columbus.

Secondary production of HCHO, though reduced during winter, may also contribute to the observed enhancements in the urban plumes. The CO, CH_4, NO_x and SO_2 tracers can also be co-emitted with AVOCs from a variety of sources that undergo photochemical oxidation to produce HCHO. The linear model analysis suggests that primary emission explain most the HCHO, accounting for just over 60% of HCHO variability, at least close the source region. The remainder of the variability may arise from a variety of sources, including primary production that correlates to other tracers not included in this model, measurement uncertainty, and

280 secondary production. The evidence for a contribution from secondary production is as follows.
281 First, although there is a strong correlation of CO to NO_x along the path of transport for plumes 1
282 – 4, there is also a decrease in the percentage of HCHO apportioned to NO_x from plume 1 – 4
283 with the tracers not following the evolution of HCHO along the path of transport. The NO_x/CO
284 enhancement ratios are 0.29 for plume 1 and 0.15 for plume 4, similar to enhancement ratios
285 attributed to vehicle traffic from within an urban region according to emissions inventories
286 conducted by *Hassler et al.* [2016]. Second, the r^2 values of 0.67 in the linear fit suggests either a
287 missing primary emission or a secondary production of HCHO that is not captured by the tracers
288 used in this analysis. The amount of secondary HCHO will be estimated using a box model
289 analysis given below.
290
291

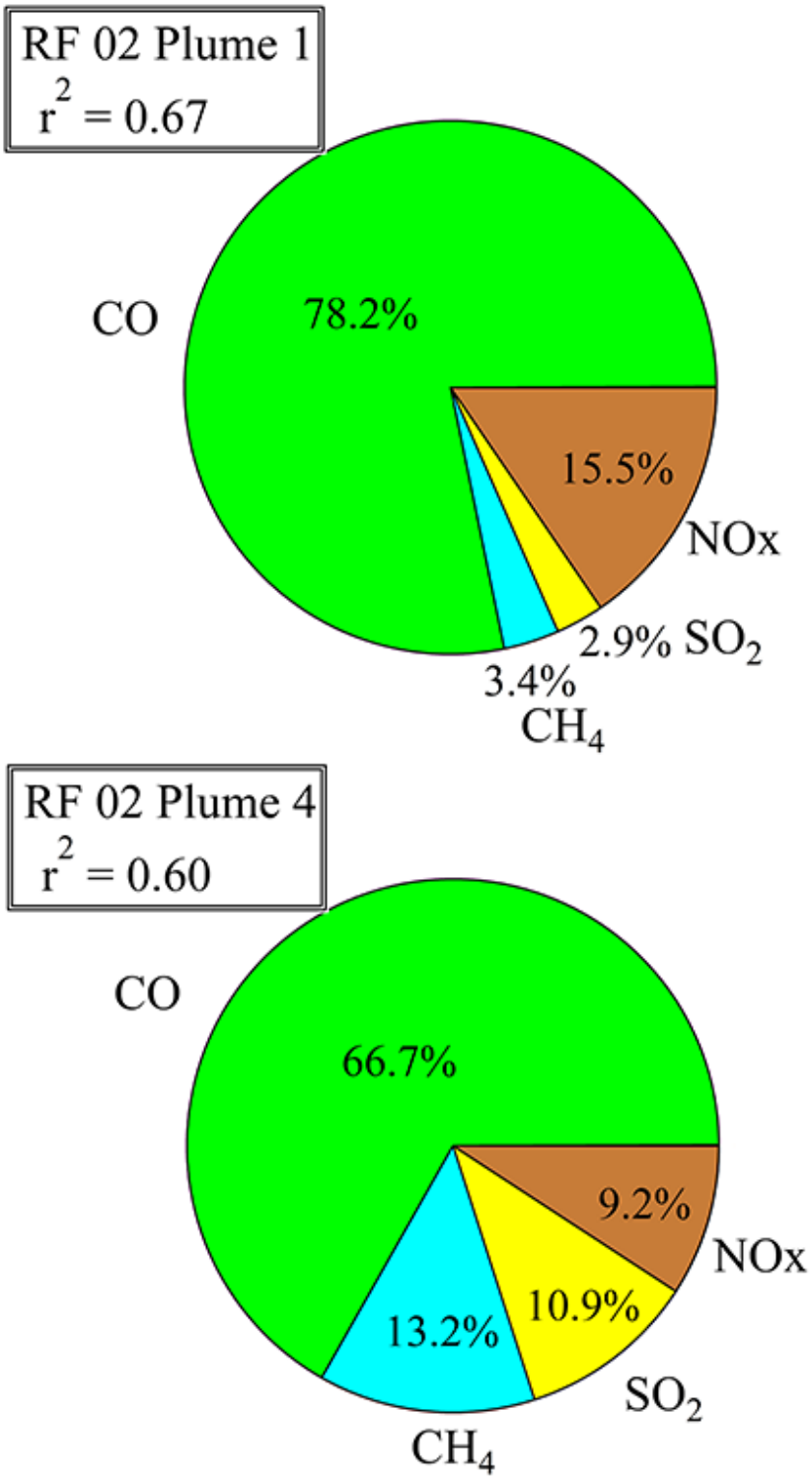


Figure 5: Linear model distribution for the chemical tracers associated with HCHO in RF 02 urban plumes. Plume 1 is close to the city center of Cincinnati, OH. Plume 4 is from Columbus, OH

292

293 To assess the relative contribution of primary and secondary HCHO sources, we examine
294 the evolution of the Cincinnati and Columbus plumes from RF02. Figure 6 shows the
295 progression of the HCHO-to-CO enhancement ratio, ΔHCHO/ΔCO, as a function of Lagrangian
296 plume age for each of the five plumes circled in Fig. 4. This ratio is calculated as the slope of an
297 ordinary least-squares fit of HCHO vs. CO for each plume. Following the first transect (~0.4h
298 downwind of Cincinnati), ΔHCHO/ΔCO increases by ~33% before decreasing gradually in the
299 next three plumes. Toluene and benzene, which do not have secondary sources, exhibits similar
300 behavior (Fig. S1). This is loosely consistent with primary emissions driving the observed
301 changes in HCHO, as opposed to strong secondary production.

302 Though oxidation is slow in the winter, it is likely that some fraction of HCHO is
303 produced through oxidation of VOC, especially alkenes. To illustrate this point, we approximate
304 the evolution of the urban plume with a 0-D photochemical box model. Here we employ the
305 Framework for 0-D Atmospheric Modeling (F0AMv4, available at
306 https://github.com/AirChem/F0AM) [*Wolfe et al.*, 2016] in combination with the Master
307 Chemical Mechanism (MCMv331) [*M Jenkin et al.*, 2015; *M E Jenkin et al.*, 1997; *Saunders et*
308 *al.*, 2003]. The model is initialized with mixing ratios from the peak of the first plume downwind
309 of Cincinnati. Chemical constraints include CH_4, CO, O_3, NO, NO_2, HONO, and a range of
310 hydrocarbons and oxidized VOC (including HCHO). The TOGA instrument does not measure
311 small alkenes, so we estimate initial mixing ratios of ethene, propene, c-2-butene, t-2-butene, and
312 1,3-butadiene by rescaling emission ratios for Los Angeles reported by *de Gouw et al.* [2017a].
313 Meteorology (P, T, RH) and photolysis frequencies are fixed at observed mean values for the
314 five plumes. Dilution is treated as first-order with a dilution constant of 1 day^{-1} and background
315 concentrations taken from observations just south of the plume intercepts. The model is

316 integrated forward in time for 6 hours. After t = 0, all chemical concentrations are determined by
317 the model except for HONO, which is constrained to observed values (50 – 100 pptv) throughout
318 the simulation to improve representation of OH (the model does not include heterogeneous
319 HONO sources). HCHO enhancement ratios are calculated as the ratio of background-subtracted
320 model HCHO and CO mixing ratios.

321 This simulation is meant to illustrate the relative contribution of secondary production to
322 the HCHO budget. As such, we divide model HCHO into two classes: "initial" HCHO (which
323 we presume is mainly from direct emissions), and "secondary" HCHO produced within the
324 plume after t = 0. This model is not designed to accurately capture all aspects of Lagrangian
325 plume evolution. Sensitivity simulations, however, indicate that results presented here are
326 insensitive to assumed photolysis frequencies or dilution rates. The median OH concentration for
327 the simulation is 4×10^5 cm^{-3}, within the range of observations under similar conditions (Stone et
328 al., 2012). We estimate an uncertainty of ±50% in model OH due to constraints and assumptions.

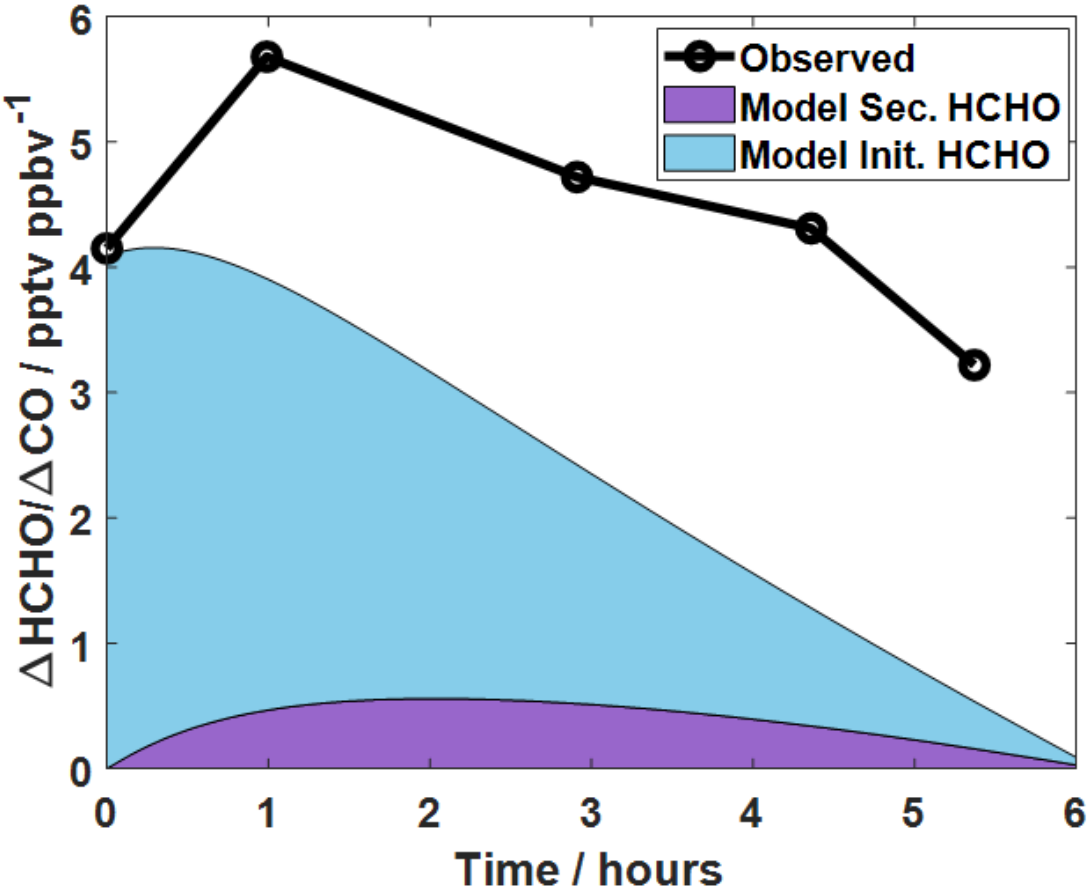


Figure 6. Comparison of observed and simulated HCHO enhancements relative to CO in the Cincinnati/Columbus plumes encountered on RF02. The thick black line/circles show the observed enhancement ratio. Colored area shows the model-simulated HCHO enhancement due to secondary production (purple) and initial HCHO (blue). Initial HCHO likely includes both primary and secondary HCHO, as the first plume encounter was 0.4 h downwind of city center.

329

330 Model results indicate moderate photochemical production of HCHO (Figure 6).
331 Integrating over the 6-hour simulation and accounting for the uncertainty in OH, we estimate that
332 secondary HCHO comprises 21 ± 10% of the model HCHO budget. It is difficult to directly
333 compare modeled and observed HCHO as aircraft sampling is only pseudo-Lagrangian (6 hours
334 of age sampled in 1 hour of flying), but results are consistent with our expectation of missing
335 HCHO sources in the model. Potential explanations include additional HCHO precursors or

direct HCHO emissions. Given the slow oxidative conditions of the wintertime atmosphere, an additional photochemical source of HCHO is a less likely explanation. Assuming a mixed layer depth of ~1 km, a regional HCHO emission flux of 0.5 – 3 x 10^{14} molecules cm^{-2} h^{-1} could explain the range of observed ΔHCHO/ΔCO. The low end of this estimate is consistent with emissions derived from analysis of nocturnal boundary layers in a different region (Sect. 3.2).

3.1.2 Analysis of Urban plumes over the New York Metropolitan Area

Plumes near the New York metropolitan area in RF03 had NO_x/NO_y ratios that were very close to 1, as in RF02. For plume 1, RF03 shown in Figure 7, if it was carried aloft from the New York area, then the start of emission was approximately 3:00 pm EST, which was 2 hours before sunset and one hour before the evening rush hour period. Urban plumes 1 - 3 show good correlations in the individual linear fits, with r^2 values of 0.7 to 0.85 for HCHO/CO, $r^2 > 0.81$ HCHO/CH_4. For plume 1, $r^2 = 0.94$ for CO/CH_4, $r^2 = 0.96$ for CO/NO_x. New York plumes have an average HCHO/CO ratio of 0.6% HCHO to CO, which is twice the value for the primary emission ratio cited by *Cowling et al.* [2007] and *Parrish et al.* [2012], and equal to the value of this ratio for urban emissions during rush hour in the summertime Houston area [*Rappenglück et al.*, 2010].

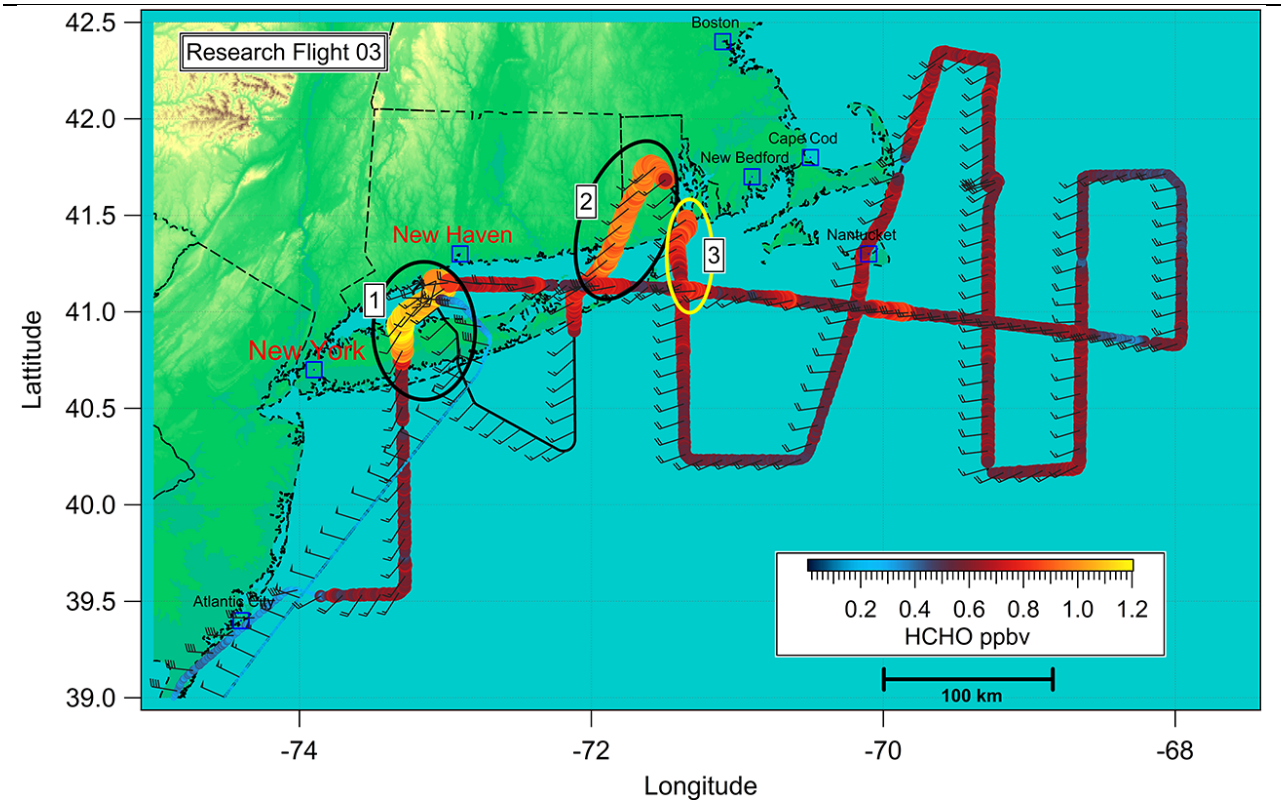


Figure 7: Research Flight 03 (RF03) on February 07, 2015. Background shading indicates terrain elevation. Each urban plume is identified by the regions enclosed in colored circles. The color of the circle indicates plumes that were attributed to the same source, with the plume in area 3 no longer undergoing photochemistry due to sunset and influenced by marine mixing. The concentration of HCHO along the flight path is indicated by the color scale and size of the marker.

352

353 Figure 8 shows the results from the linear model for plume 1, Figure 7 in RF03, which
354 was closest to New York City (r^2 ranging from 0.85 - 0.89 for the multivariable fit). Combined
355 with timing of when these plumes exited the urban area, the linear model shows that 43% of
356 HCHO production is linked to methane, 23.4% to CO, 27.1% to NO_x, and 6.5% to SO_2
357 emissions. The NY city correlation plots of plume 1, shown in Figure 3, is distinct from the cities
358 in Ohio, showing that there is a much larger contribution of CH_4, possibly from vehicles and/or
359 home heating, as it corresponds to the highest NO_x mixing ratios of 10 - 20 ppbv over NY city.
360 Unlike the urban region in the vicinity of Columbus, the $r^2 > 0.81$ for HCHO to CH_4 shows that

HCHO emissions in New York were strongly correlated with CH_4. However, the contribution of NO_x is also much higher than what was seen in either urban plume in RF02. SO_2 measurements for the region ranges from 3 -5 ppbv with no apparent evidence of coal fired power plant emissions.

The majority combustion products from the vehicular fleet in NY originate from ethanol enriched fuels (E10 – E85) during the wintertime [*Brito et al.*, 2015; *Clairotte et al.*, 2013; *He et al.*, 2009; *Knoll et al.*, 2009]. These products of combustion include formaldehyde, acetaldehyde, NO_x, other AVOCs, and the emission of unburned ethanol which can photochemically react and decompose into acetaldehyde, peroxyacetylnitrate (PAN), formaldehyde, and ozone [*Carr et al.*, 2011; *Dardiotis et al.*, 2015; *Dominutti et al.*, 2016; *Timonen et al.*, 2017]. These combustion products are also generated by fuels used in domestic heating and can result in photochemical products. In this work, observations do not include tracers needed to unambiguously separate of the total contribution of HCHO by vehicles and the contribution from home heating.

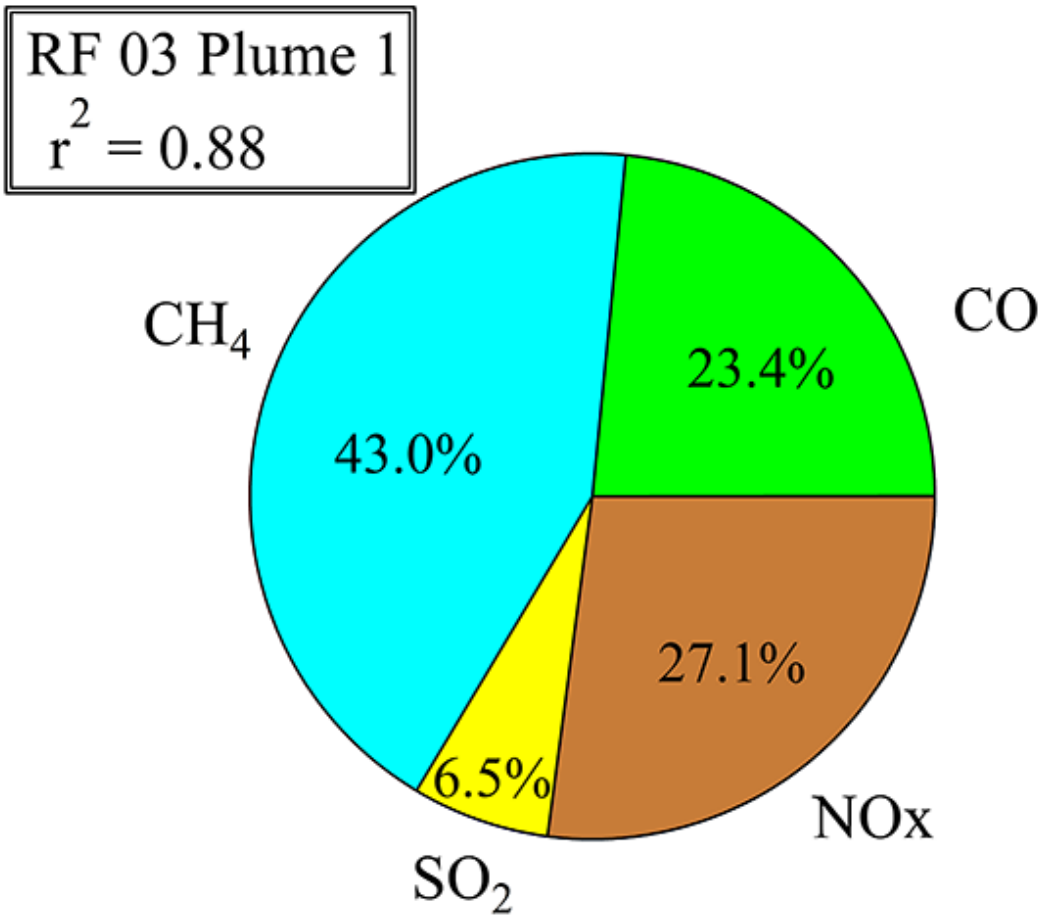


Figure 8: Linear model distribution for the chemical tracers associated with HCHO from a RF 03 Urban plume; plume 1 20 km downwind of the center of New York City.

374

375 3.1.3 Point sources of HCHO.

376 Direct emissions of HCHO may explain the presence of two large plumes in Southern
377 Ohio. In Figure 4 (RF 02), two plumes showed evidence of emissions from a point source, in a
378 region where there was no power generating station with no associated tracers (NO_x, NO_y, SO_2,
379 CH_4) correlated with the plume or associated with an EPA reporting facility, with an average
380 [HCHO] of 1.0 ppbv and a maximum value of [HCHO] 3.4 ppbv. The plume is encountered
381 again with an average [HCHO] of 1.2 ppbv and a maximum [HCHO] of 2.3 ppbv over a broader

area from the initial point of detection 146 km away, with an estimated travel time of 3.6 hours. The correlation of HCHO to CO, CH_4, SO_2, NO_x, and NO_y produced $r^2 < 0.15$, in plumes 5 and plume 9 (see Figure 4) with the exception of CO in plume 9, which had a HCHO/CO correlation of $r^2 = 0.46$, and methane near background levels in the range of 1.89 – 1.9 ppmv at both points. The lack of correlation to the tracers associated with urban emissions and low concentration of methane is not consistent with urban areas or areas where combustion of fossil fuels is occurring. This shows some evidence of a missing source AVOCs or direct emissions contributing to HCHO.

Compared to other studies, the 0.2 – 0.5% HCHO/CO ratios found in RF02 are within the range of 0.18 – 0.30% for urban emissions by vehicular traffic observed by *Cowling et al.* [2007] and higher than the 0.10 - 0.14% for urban emissions by *Anderson et al.* [1996]. These values approach the values found in the summertime expected mixing ratio enhancements from primary emissions of HCHO and CO from vehicular traffic ratio of 0.3 % given during the summer by *Parrish et al.* [2012] and 0.6% by *Rappenglück et al*. [2010]. Given the chemical box model used in this work suggests secondary HCHO to account for 21 +10 % of the observed HCHO well downwind of urban areas in winter conditions with low BVOC, the observed HCHO/CO ratios may be regarded as modest upper limits to the primary emission ratios in the presence of unknown point sources.

3.2 Night time urban emissions

The data collected during RF07 provides an opportunity to constrain regional HCHO emission using a budget-based approach for the nocturnal boundary layer (NBL). For this analysis, we assume that the residual layer (RL) represents NBL conditions at sunset (time = 0),

and that any difference between the NBL and RL is due to surface emissions of HCHO. In addition, several assumptions were made in the analysis: (1) the residual layer and nocturnal layer are stable and are mostly uncoupled, (2) nighttime chemical production/loss and dry deposition of HCHO is negligible, and (3) there is relatively minor variability in horizontal advection, such that we can treat the nocturnal boundary layer as a well-mixed and uniform box. As shown in Figure S2, several small airports were selected to perform multiple missed approaches (MAs). These missed approaches were used to ascertain the altitude of the boundary, residual, and nocturnal layers and to determine if these layers remained stable through the night as shown in Figure 9. During RF07, the vertical thickness of the nocturnal layer ranged between 150 – 200 meters, and residual layer was 500 – 700 meters. Relative humidity through the nocturnal and residual layers remained around 30 – 40% and rapidly decreased above the boundary layer. Characteristics of each of the missed approaches with stable layers allowed for further analysis to estimate the emissions from the ground into the nocturnal layer.

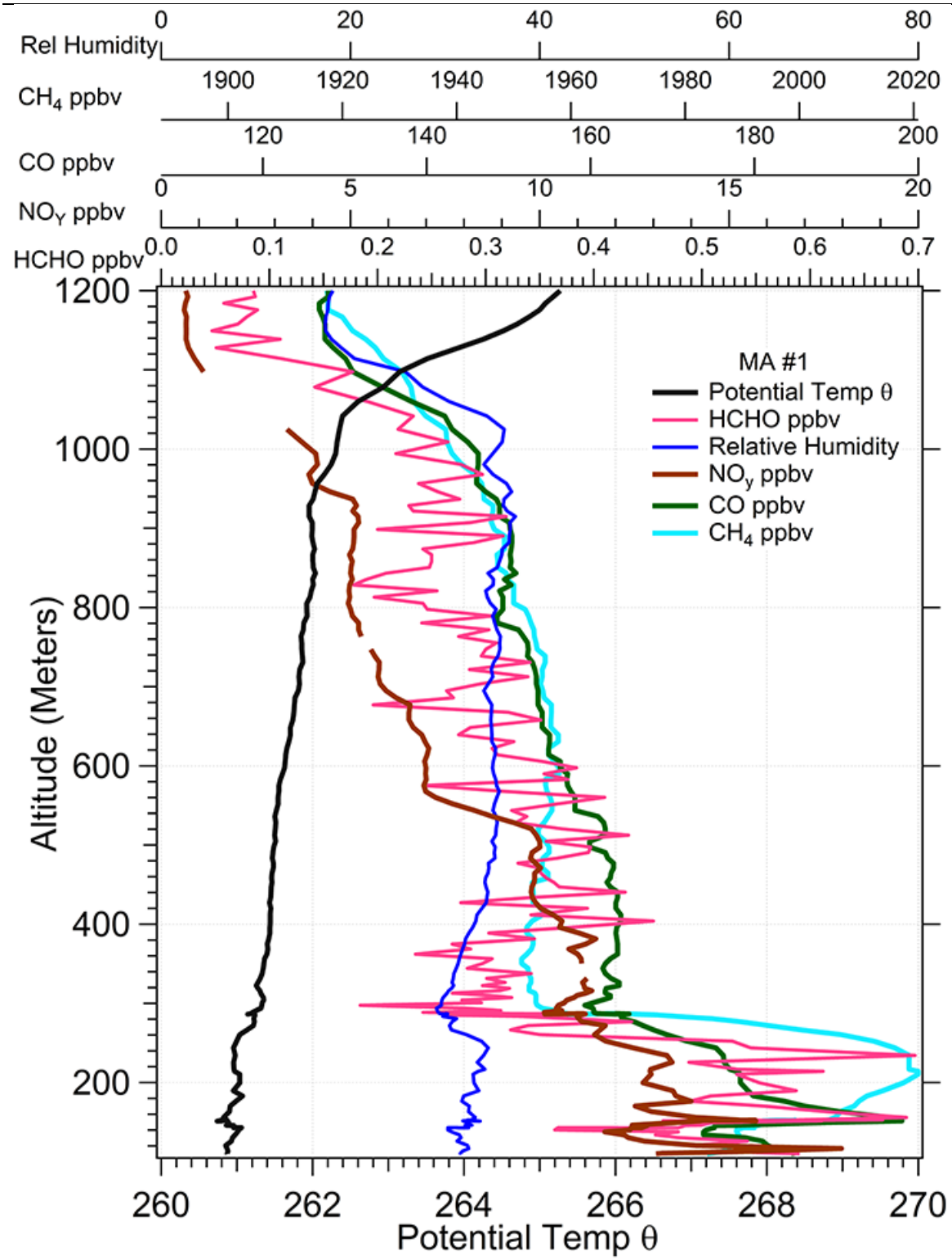


Figure 9: Vertical profile of potential temperature (black), relative humidity (blue), and several chemical tracers obtained during a nocturnal missed approach near Chambersburg, PA on RF07. Two locations where suitable data for this analysis was obtained was at air ports outside of Chambersburg, PA and Harrisburg, PA.

417

418 In Equation 3, the difference in the concentration of HCHO, [HCHO] (molecules cm^{-3}) of
419 nocturnal and residual layers was defined as Δ[HCHO] and was then multiplied by the number
420 density of air (M) and the column-integrated concentration of HCHO within the nocturnal layer
421 (Ω_{HCHO}, molecules cm^{-2}) which was found using the nocturnal boundary layer height (H) for
422 each missed approach, as defined in Equation 4. The resulting value of Ω_{HCHO} represents a
423 column measurement of [HCHO] emitted from the ground to the nocturnal layer compared to the
424 amount in the residual layer. When these are plotted vs. time since sunset, this gives the flux of
425 HCHO emitted from the area in molecules cm^{-2} hr^{-1}.

(3) $$\Delta[HCHO] = [HCHO]_{residual} - [HCHO]_{nocturnal}$$

(4) $$\Omega_{HCHO}\ (molecules/cm^2) = \Delta[HCHO] \times H_{boundary\ layer} \times \mathrm{M}$$

426 Using the data collected from the ascending and descending legs of MA 1, 2, and 7
427 (shown in Figure S2), Ω_{HCHO} is plotted against time since sunset to determine the HCHO
428 emission flux into the NBL, as shown in Figure 10. Based on average Δ[HCHO] values, the
429 average HCHO column growth rate is $(1.1 \pm 0.3) \times 10^{14}$ molecules cm^{-2} hr^{-1} (1σ uncertainty).
430 Using Δ[HCHO] values based on the maximum [HCHO] measured in each layer, an emission
431 flux of $(1.3 \pm 0.2) \times 10^{14}$ molecules cm^{-2} hr^{-1} is found.

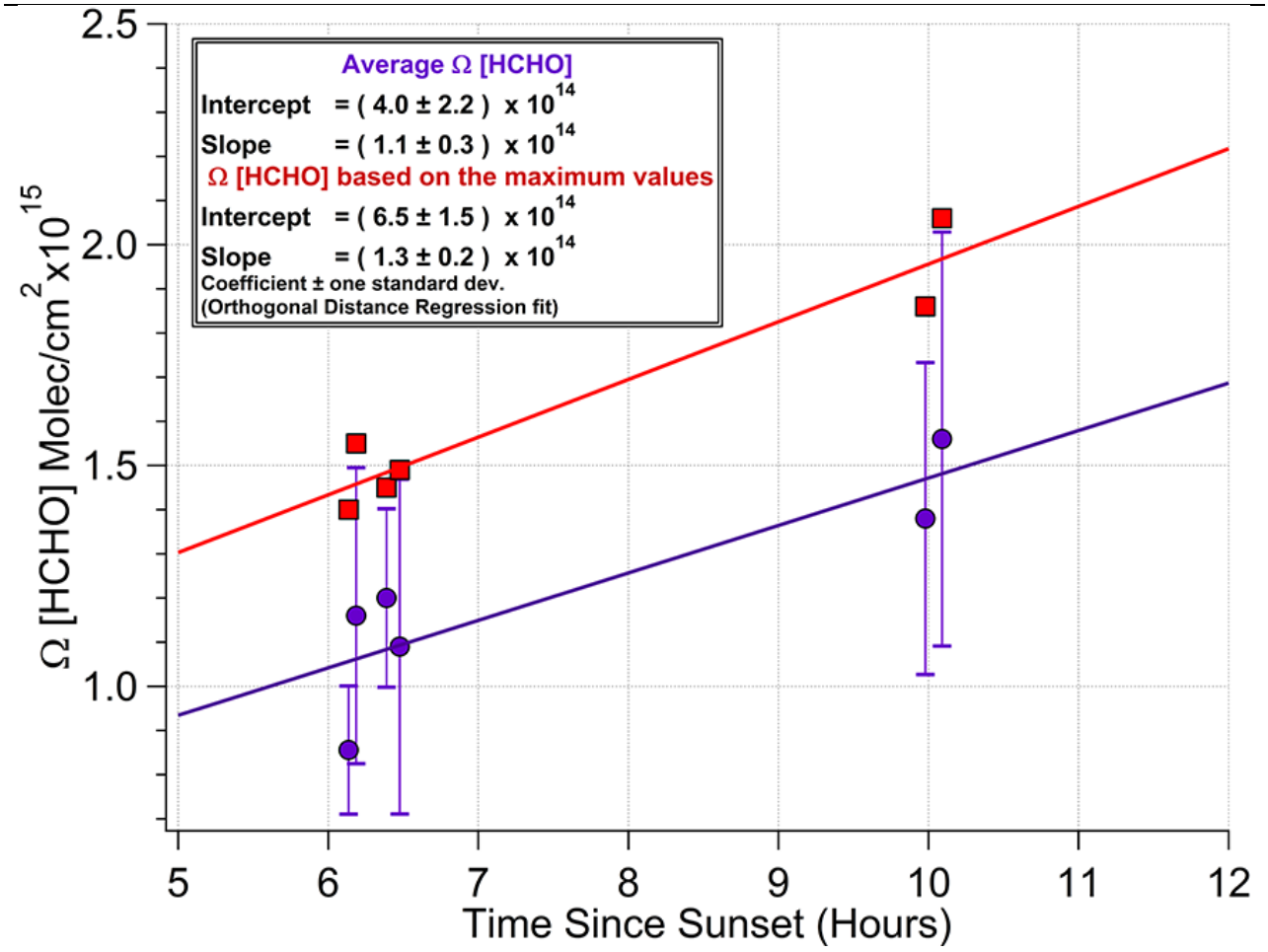


Figure 10. A plot of Ω_{HCHO} vs. time since sunset for missed approaches in RF 07. The average Ω_{HCHO} vs. time is in purple while the based on the maximum Ω_{HCHO} vs. time is based on the maximum HCHO in each of the layers encountered is in red.

Output from the reference and improved GEOS-Chem (v10-01) 3D model simulations sampled along the flight tracks was compared to the results found in Figure 10 [*Shah et al.*, 2018]. Ω_{HCHO} values from GEOS-Chem were determined in a similar manner as the experimental measurements based on missed approach data, and both used the observed boundary layer height, since the vertical resolution of GEOS-Chem was insufficient to determine the height. The maximum HCHO emission flux from area sources was inputted into GEOS-Chem, using the NEI 2011 database scaled to 2015 using the improved simulation set from

Jaeglé et al. [2018] featuring the 5x scaling for HCHO based on observational data around the three areas of the missed approaches, with 5.1×10^{13} molecules $cm^{-2}hr^{-1}$ at point 1 and 1.3×10^{14} molecules.$cm^{-2}hr^{-1}$ at points 2 and 7 (See Figure S2) using a 50 km × 50 km grid. Compared to the values of the average Ω_{HCHO} of 1.1×10^{14} molecules $cm^{-2}hr^{-1}$ and the max Ω_{HCHO} of 1.3×10^{14} molecules $cm^{-2}hr^{-1}$ found using the flight data, the scaled NEI input at point 1 is about a factor of 2 lower, while at points 2, 7 the input is near to both values of average and maximum Ω_{HCHO}. When emissions into the nocturnal boundary layer based on the GEOS-Chem output along the flight track was examined, the average emissions flux was $(9.9 \pm 1.7) \times 10^{14}$ molecules $cm^{-2}hr^{-1}$, 9 times larger than the measured average Ω_{HCHO} and 7.6 times larger than the max Ω_{HCHO}. However, this is an inaccurate comparison for several reasons. In GEOS-Chem, the space within 0 to 3 km altitude contains 17 layers to compute the concentration of the chemical species, where the average concentration is calculated in a volume using the vertical height of the individual layer and the grid dimensions as a base. Each of the vertical heights is determined by the pressure in the atmospheric column from sea level to 80km (a total of 72 layers) based on the GEOS-FP, "forward processing," meteorological data products. From the pressure altitude of 0 to 1000 meters, or at a ceiling of 900 meters' altitude in the profile in Figure 9, would only contain 7 of these layers in GEOS-Chem. Consequently, there are fewer data points available in GEOS-Chem for averaging compared to the 50 to 100 points in the aircraft data. The result is still an improvement compared to the reference simulation done by *Jaeglé et al.* [2018] without any adjustment. The Ω_{HCHO} taken from the GEOS-Chem reference simulation output was $(5 \pm 2) \times 10^{12}$ molecules $cm^{-2}hr^{-1}$, 22 times smaller than the measured average Ω_{HCHO} of 1.1×10^{14} molecules cm^{-2} hr^{-1} and 26 times smaller than the max Ω_{HCHO} of 1.3×10^{14} molecules cm^{-2} hr^{-1}. It

462 is apparent that work is still needed to reduce the underestimation of the NEI emissions fluxes of
463 HCHO to produce results that match observed [HCHO] in finer detail.

464 3.2.1 Nocturnal emissions near Atlanta, GA

465 Atlanta, Georgia lies in the southern U.S., a different region than sampled by the majority
466 of WINTER research flights in the northeast U.S. Unlike the northeast, the southern U.S. has
467 significant biogenic emissions, such as monoterpenes, even during the winter months [*Hagerman*
468 *et al.*, 1997]. RF10, sampled the residual layer over and downwind of Atlanta, with a series of
469 profiles through the nighttime boundary layer structure through missed approaches to airfields.
470 Formaldehyde sampled in the residual layer showed evidence for mixing between direct
471 emissions from the urban area together with secondary production. Due to the presence of
472 monoterpenes during winter in the southern U.S., a larger secondary component to HCHO may
473 be expected, though such chemistry is likely oxidant-limited.

474 The plumes in the residual layer on RF10 can be separated into two categories. The first
475 category, (plumes 1, 3, 4, 5, 9, and 10 in RF10, numbers in Figure S3) contains plumes in which
476 HCHO is highly correlated with CH_4 and CO. Values for the correlation coefficient of HCHO
477 with CO range between $0.94 > r^2 > 0.88$, and correlation with HCHO to CH_4 range between 0.89
478 $> r^2 > 0.79$. The individual contributions of co-emission of HCHO with either CH_4 or CO are
479 difficult to separate due to the strong correlation of CH_4 with CO. While we retain this
480 separation in this analysis, we recognize that the analysis may not accurately provide a separate
481 attribution to each. The ratio of HCHO/CO ranges between 0.6 % to 1.8%, and averaging at a
482 ratio 1.7%, and the HCHO/CH_4 ratio ranges between 0.5% to 1.2 %, averaging at a ratio of 1.1%.
483 Common to this group is NO_x mixing ratios ranging between 0.5 and 6 ppbv, NO_y ranging

484 between 1 and 8 ppbv, and a peak amount of HCHO of 0.65 – 1.1 ppbv. These plumes are also
485 characterized by O_3 mixing ratios of 30 – 40 ppbv and CO from 120 ppbv – 160 ppbv. Plumes 1
486 and 3 in RF10 contained $NO_x < 0.5$ and $NO_y < 1.5$, with plume 1 intercepted at an altitude of 120
487 m above ground during a missed approach; see Figure S3 and Figure S4. The second category of
488 HCHO plumes, numbered 2, 6, 7, and 8, 11, and 12 seen in black in Figure S3, are plumes in the
489 residual layer and have much weaker HCHO correlations with other species. The r^2 values are in
490 the range of $0.03 > r^2 > 0.15$ for HCHO vs CO, $0.26 > r^2 > 0.01$ for HCHO vs CH_4, and $0.44 > r^2$
491 > 0.19 for HCHO vs NO_y. The plumes were intercepted in the range of 430 – 580 meters above
492 ground. These contain CO in the ranges of 160 – 200 ppbv, with a peak mixing ratios of HCHO
493 of 0.7 – 1.1 ppbv, like the HCHO in the first category. The region containing plumes 9 - 12 show
494 evidence of significant mixing of the plumes from both categories. The region containing Plumes
495 2 - 4 also show a similar pattern of mixing but it is not as visible as the example in Figure 11.

496 The plots in Figure 11 combine plumes 9 – 12 in order to show the change in the slope of
497 HCHO/CO, HCHO/NO_y and O_3/HCHO as the aircraft samples a series of plumes that exhibit
498 either dominantly direct emissions or direct emissions influenced by photochemistry from the
499 previous day. The mixing between these two air masses is marked by the increased mixing ratio
500 of CO and NO_y and the decreased mixing ratio of O_3.

501 At high values of CO (180 – 230 ppbv), the slope of formaldehyde vs CO is 0.2%, similar
502 to the value quoted for direct urban emissions from other studies [*Parrish et al.*, 2012],
503 indicating that at these more concentrated levels the primary contribution to observed HCHO is
504 direct emission. At lower values of CO (125 – 150 ppbv) the corresponding slope is much
505 steeper, at 1.7%. This higher value is likely to be dominated by secondary, photochemical
506 production of HCHO in more dilute urban pollution that was emitted the previous day and is

present in the residual layer on this nighttime flight. Mixing between these two air masses produces a range of points at intermediate CO (150 < CO < 180 ppbv) that falls below the extrapolated fits to either of the high or low range of CO but that creates a mixing line that connects the two populations. The distribution of HCHO against NO_y (an approximately conserved tracer for the emission of NO_x) shows a similar behavior, with slopes given in the figure. Evidence for this interpretation can be seen in the relationships between O_3 vs CO and O_3 vs HCHO in plots C and D in Figure 11. Although the overall relationship between O_3 and CO shows an anti-correlation, at higher mixing ratios of CO, the slope of O_3 vs CO is relatively steeper than it is at low CO. A similar relationship exists in a plot of O_3 vs NO_y. The overall anti-correlation in this plot indicates that the urban emissions are overall ozone-destroying, likely dominated by NO_x titration, in this winter environment. However, the points at lower CO have a reduced O_3-CO slope, indicating that the destruction is moderated by photochemical O_3 production in these points, consistent with the presence of a higher HCHO-CO slope from secondary HCHO production in this population of points. Similarly, the relationship between O_3 and HCHO exhibits an overall anti-correlation, but with a steeper slope at high CO than at low CO.

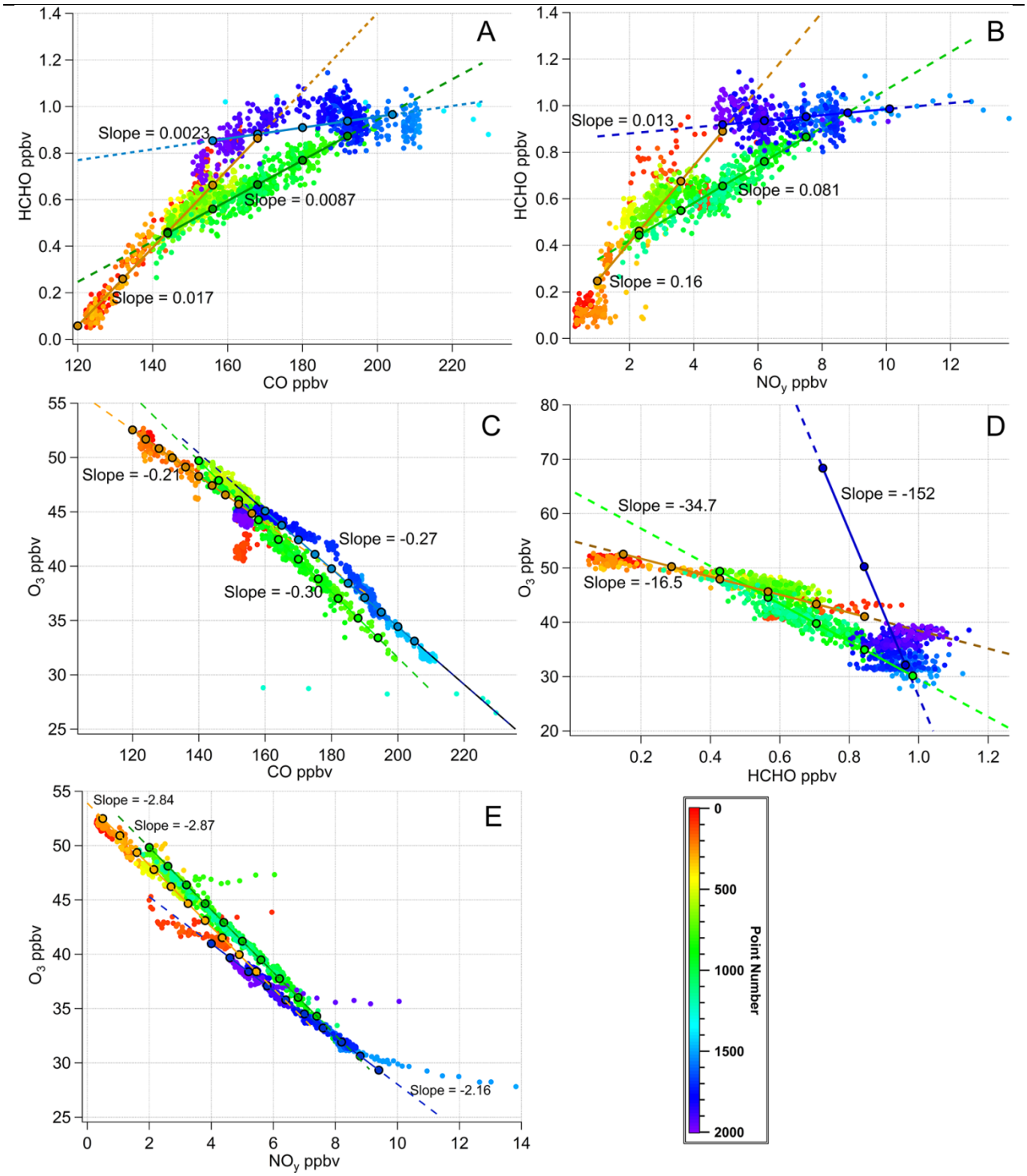


Figure 11: Four plots of the combined plumes 9 – 12 for RF10. The color spectrum moves from orange to blue along with increase in data points as aircraft passed through group of air masses encountered during RF10 occurring between 4:40 – 5:10 am EDT (9:40 and 10:10 UTC), shown in the color scale bottom right. A. The combined plot of HCHO vs CO describes the distinct air masses in terms the HCHO/CO ratio, showing a steep slope at low CO and a shallow slope at high CO, as described in the text. B. Shows the combined plot for HCHO vs. NOy. C. O_3 vs. CO anti-correlated with small range in

slope with increasing CO. D. Combined plot of O_3 vs. HCHO relationship is anti-correlated, with a steeper slope at high CO as described in the text. E. The combined plot O_3 vs. NOy.

523

524 3.3 Point source emissions of HCHO

525 Several instances of elevated HCHO (0.75 – 6.6 ppbv) were observed in close proximity
526 to power stations in RF04 and 07. The area covered by RF04 and RF07 (Figures S5 and S6)
527 includes several coal, natural gas, and diesel co-generating power stations. Generating stations
528 that utilize both natural gas and diesel (various bio-diesel) fuel types, separately or
529 simultaneously, generate HCHO through the combustion of diesel oil [*Basha et al.*, 2009; *He et*
530 *al.*, 2009; *Lehto et al.*, 2014]. Other power stations that are co-generating facilities utilize wood,
531 refuse, and coal, and they may also emit HCHO.

532 In RF04, Figure S5, the LV Sutton power station was identified as a combined cycle
533 power station using natural gas and diesel, producing a direct emission of HCHO. The top of
534 Figure 12 shows that power station emissions at ~1:54 AM overlap, with the spike of HCHO
535 coming from an exhaust stack dedicated to diesel, and the other profile coming from natural gas.
536 Because there is no direct measurement for CO in the CEMS database, CO_2 must be relied upon
537 to identify the power plant. Since VA Renewable Portsmouth station had the greatest magnitude
538 of CO_2 emissions reported from CEMS database that matches the measured CO_2 emission, it is
539 the only station in operation that the measured HCHO of 0.75 ppbv, can be attributed to. Given
540 the wind direction, several power plants could produce plume 1 (see Figure S6), which reached a
541 maximum of 0.75 ppbv HCHO. Since VA Renewable Portsmouth station was a far larger emitter
542 of CO_2, according to the CEMS database, it is the likely producer of plume 1. One source
543 measured at 1:52 UTC showed significant quantities of CO and HCHO, while a larger peak in

HCHO measured at 1:53 UTC was co-emitted with significant quantities of CO and CO_2. There was a very good correlation, (r^2 = 0.91) for HCHO and CO, and the HCHO/CO ratio of 1.8% from the power station (the bottom panel of Figure 12). This ratio was higher by a factor of ~2.3 when compared to the NEI (2014) aggregate emissions ratio of 0.80% HCHO/CO and the NEI (2017) value of 0.76%. A maximum of 6.126 ppbv HCHO was measured for the L.V. Sutton plume, with the amount of CO_2 from another combustion source from the same power station since the plant utilizes natural gas and diesel fuels.

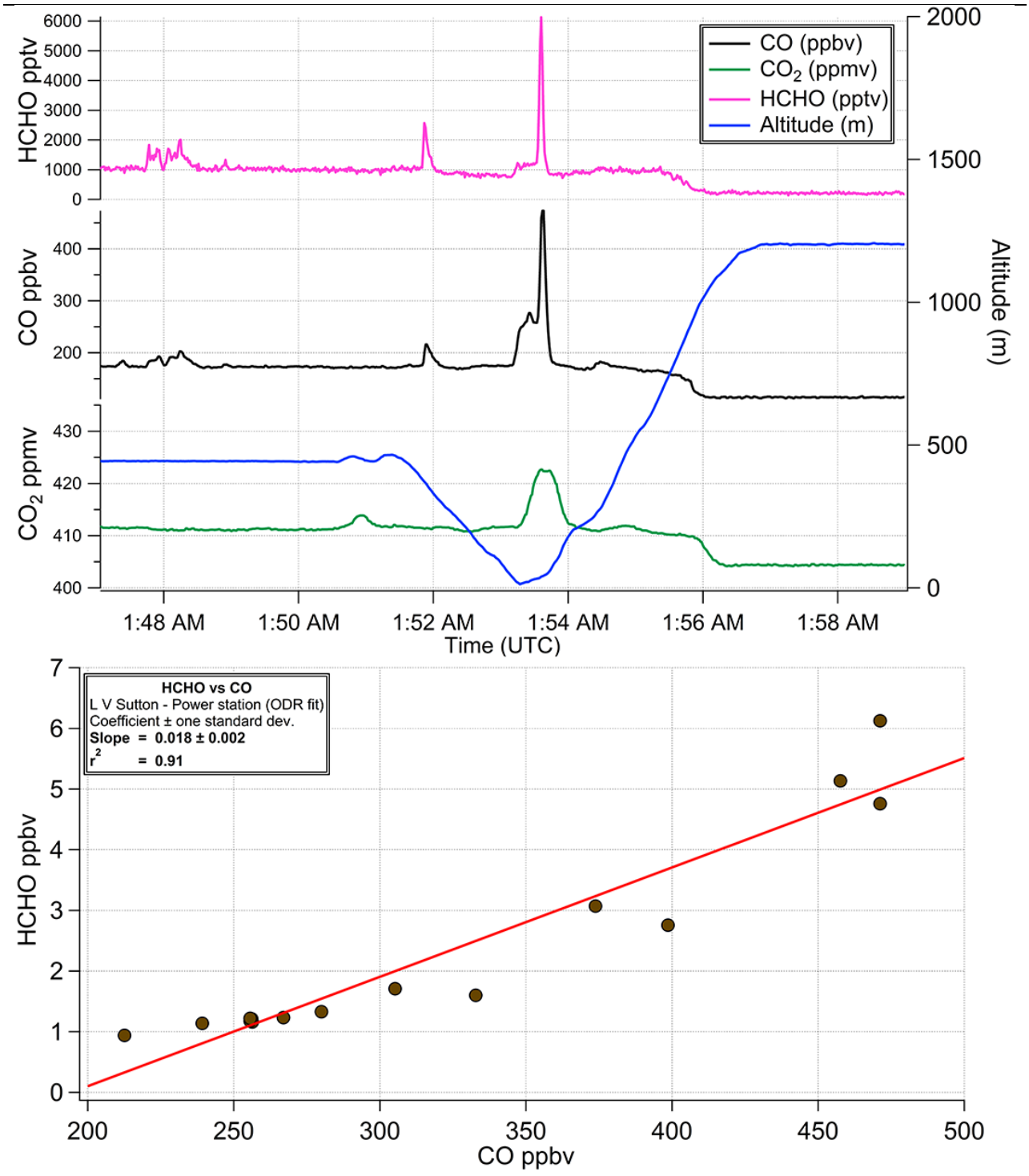


Figure 12: An example of emissions from a co-generating power station producing direct emission of HCHO. (Bottom Left) L.V. Sutton power station in North Carolina, operating using both natural gas and diesel fuels produce emissions.

551

552 Another co-generating power station in RF07, Figure S6, Va. Renewable Portsmouth
553 LLC, had a similar HCHO/CO ratio of 1.7%, (r^2 = 0.71) but was more obscured by other
554 emissions from either the same power station or emissions from the Elizabeth River power
555 station. The NEI (2014) and NEI (2017) aggregate HCHO/CO emissions ratio for Va.
556 Renewable Portsmouth LLC was 0.0035% and 0.11%. The measured ratio is 15 times greater the
557 NEI (2017) value for HCHO/CO. Sunrise occurred during RF07 at 11:43 AM UTC (centered on
558 Norfolk, VA), 7 minutes after the measurement, so it is unlikely that photochemistry reduced
559 HCHO mixing ratio during the plumes time aloft. The mixing ratios observed from both power
560 generating stations are well in excess of typical urban plumes from the WINTER campaign, with
561 levels of CO approaching 400 ppbv.

562 As mentioned earlier, HCHO scaling was needed to bring the NEI data input into the
563 GEOS-Chem model close to the in-situ observations from aboard the aircraft [*Shah et al.*, 2018].
564 Here we have a similar factor of underestimation when NEI was used directly to compare, under
565 conditions without secondary production (i.e., nighttime emissions). The emissions ratios
566 determined from the measured data are 2.3 - 15 times greater than the annual estimates from the
567 NEI 2017 emissions database. Also, the available databases for the CEMS and NEI do not
568 provide an estimate of the daily or monthly emissions of HCHO during facility operation for
569 comparison, so lacks any variation on small time scales. Figure S7 displays the NEI 2017 yearly
570 estimated emissions level per state in the US. Table S1 the HCHO/CO ratio for all the identified
571 plumes. Models that utilize the NEI database may underestimate HCHO emissions from power
572 stations, or they may be limited by the reported information in the database. For example, there
573 is no category in the NEI for diesel fueled combined power station, where other types such as
574 wood, coal, and natural gas are covered. This may explain a part of the HCHO not accounted for

575 in models, as diesel combustion and hydrocarbon products from diesel combustion, and other
576 possible AVOC emissions are not included.

577 **4. Conclusions**

578 We report the wintertime aircraft observations of HCHO from the near urban areas in the
579 Eastern U.S. from the WINTER campaign carried out on the NSF C130 between February and
580 March 2015. This is a unique data set for assessing the spatial distribution of HCHO in the
581 winter season. Due to much slower chemical production of secondary HCHO during the winter,
582 these measurements are more sensitive to the primary emission sources of HCHO and improve
583 the accuracy of primary HCHO emission ratios to other pollutants, such as CO, from urban areas
584 and point sources. They can be further used to assess the rates of wintertime photochemistry.

585 Urban regions in Ohio, New York, Atlanta, GA, Virginia, and North Carolina exhibit
586 both area and point source emissions of HCHO. Daytime ratios of urban HCHO/CO range
587 between 0.22% – 0.50% for the Ohio area with plumes experiencing aging over 6 hours, and
588 0.57% – 0.60% for plumes from New York and Connecticut urban areas experiencing aging of
589 less than 2 hours. The analysis from the multivariate linear model used to compare the regions in
590 Ohio to New York City suggests that timing of vehicular activity may be correlated to the direct
591 emission of HCHO. Other anthropogenic emissions within the region also contribute to
592 secondary production of HCHO. The linear model applied to the urban plume closest to New
593 York had a higher r^2, from 85 – 89, indicating that the tracers considered account for this fraction
594 of variability in HCHO.

595 Model calculations of AVOC oxidation rates provide estimates of the relative
596 contribution of secondary production and primary emission of HCHO. While the correlation of

HCHO to other primary emissions in Ohio, shown in Figure 5, can account for up to 67% of the variance in HCHO, a box model shown in Figure 6 shows that 30% of the observed HCHO could be attributable to secondary production after 6 hours of transport, but smaller fractions near the source regions. It is likely that both primary emissions and secondary chemistry contribute to the HCHO budget in urban-influenced regions, despite the relatively slow rate of winter photochemistry. Nevertheless, the analysis indicates primary emissions to be the major contribution to HCHO in the northeast U.S. during winter.

Night flights sampling the urban areas and surrounding regions in Virginia and Georgia characterized HCHO emissions and mixing with photochemically produced HCHO. In the region around Atlanta, GA, plumes sample at night in the residual layer showed evidence for mixing between direct urban emissions and photochemical production of HCHO from the preceding day. The urban emissions over nighttime Atlanta are overall ozone-destroying, likely dominated by NO_x titration, with HCHO and O_3 anti-correlated with each other. Other large localized sources of HCHO, such as the power stations and other area sources and point sources were intercepted by multiple missed approaches in VA. Sampled area sources in VA during the night, emitted an average of $(1.1 \pm 0.3) \times 10^{14}$ molecules $cm^{-2}hr^{-1}$ or a maximum of $(1.3 \pm 0.2) \times 10^{14}$ molecules $cm^{-2}hr^{-1}$ of HCHO based on measurements taken from the nocturnal and residual layers and the time since sunset in the region.

Two-point source emissions during RF 02 in Ohio produced plumes with large HCHO mixing ratios, with average and maximum values of 1.04 – 1.18 and 2.25 – 3.39 ppbv, respectively. Two direct emissions of HCHO were identified from natural gas/diesel co-generating power stations on RF 04 and RF 07: L.V. Sutton, correlation $r^2 = 0.98$ for HCHO and CO, ratio of HCHO/CO of 1.8% with a maximum observed concentration of 6.126 ppbv HCHO,

and Va. Renewable Portsmouth LLC, HCHO/CO ratio of 0.017 and maximum observed concentration of 0.75 ppbv HCHO. For these emitters, very little or no reported information is available for comparison to their estimated points of origin of the measurements from these intercepted plumes. The NEI aggregate data is only resolved on an annual basis, and by directly comparing the NEI emission ratio of HCHO/CO for the 2017 year, it was found that emissions ratio for the power station was underestimated by a factor of 2.3. Diesel fueled power generation is also not a category in the NEI, resulting in the exclusion of AVOC product generated by diesel. Other factors leading to potentially inaccurate HCHO emission factors include excluding items such as operating load and operational time. With no daily or monthly reported values from either the CEMS or NEI, models that rely on NEI data may inaccurately represent HCHO during the winter season. As a result, HCHO emissions may have been underestimated in any previous work that utilized reported data, or have used in situ measurements of other species and emission ratios to extrapolate HCHO, which results in its underestimation, as shown in *Luecken et al.* [2012] and *Zhu et al.* [2017].

Acknowledgments and Data

The authors thank Samuel Hall, and Kirk Ullman from the National Center of Atmospheric Research (NCAR) for the limited use of the data obtained from the HIAPER Atmospheric Radiation Package. The authors also thank Andrew Weinhiemer and Denise Montzka from NCAR for the supplementary use of the oxidized nitrogen species and ozone data obtained during the winter campaign. The authors acknowledge the NSF-NCAR Research Aircraft Facility engineers, scientists, pilots, and staff members. Funding for NCAT group

642 participation was made possible by funding from NSF award to Thornton and Jaegle # NSF
643 AGS-1360745.

644 EPA Air Markets Program Data available at https://www.epa.gov/air-emissions-
645 inventories/2017-national-emissions-inventory-nei-data. Data obtained from the WINTER C-130
646 research flights used in this study is available at http://data.eol.ucar.edu/project/WINTER.

647

648

649

650

651

652

653

654

655

656

657

658

659

660

661

662 **References**

663 Alzueta, M. U., and P. Glarborg (2003), Formation and destruction of CH2O in the exhaust
664 system of a gas engine, *Environmental science & technology*, *37*(19), 4512-4516.
665
666 Anderson, L. G., J. A. Lanning, R. Barrell, J. Miyagishima, R. H. Jones, and P. Wolfe (1996),
667 Sources and sinks of formaldehyde and acetaldehyde: An analysis of Denver's ambient
668 concentration data, *Atmospheric Environment*, *30*(12), 2113-2123.
669
670 Apel, E., R. Hornbrook, A. Hills, N. Blake, M. Barth, A. Weinheimer, C. Cantrell, S. Rutledge,
671 B. Basarab, and J. Crawford (2015), Upper tropospheric ozone production from lightning NOx-
672 impacted convection: Smoke ingestion case study from the DC3 campaign, *Journal of*
673 *Geophysical Research: Atmospheres*, *120*(6), 2505-2523.
674
675 Bai, Y. Du, A. Seagram, and K. Craig (2017), MOVES-based NOx analyses for urban case
676 studies in Texas, paper presented at International Emission Inventory Conference, Baltimore,
677 MD, August.
678
679 Bai, J., G. de Leeuw, I. De Smedt, N. Theys, M. Van Roozendael, L. Sogacheva, and W. Chai
680 (2018), Variations and photochemical transformations of atmospheric constituents in North
681 China, *Atmospheric Environment*, *189*, 213-226.
682
683 Basha, S. A., K. R. Gopal, and S. Jebaraj (2009), A review on biodiesel production, combustion,
684 emissions and performance, *Renewable and sustainable energy reviews*, *13*(6-7), 1628-1634.
685
686 Brito, J., F. Wurm, A. M. Yáñez-Serrano, J. o. V. de Assunção, J. M. Godoy, and P. Artaxo
687 (2015), Vehicular emission ratios of VOCs in a megacity impacted by extensive ethanol use:
688 results of ambient measurements in Sao Paulo, Brazil, *Environmental science & technology*,
689 *49*(19), 11381-11387.
690
691 Brown, S., H. An, M. Lee, J.-H. Park, S.-D. Lee, D. L. Fibiger, E. E. McDuffie, W. P. Dubé, N.
692 L. Wagner, and K.-E. Min (2017), Cavity enhanced spectroscopy for measurement of nitrogen
693 oxides in the Anthropocene: results from the Seoul tower during MAPS 2015, *Faraday*
694 *discussions*, *200*, 529-557.
695
696 Carr, S. A., M. A. Blitz, and P. W. Seakins (2011), Site-specific rate coefficients for reaction of
697 OH with ethanol from 298 to 900 K, *The Journal of Physical Chemistry A*, *115*(15), 3335-3345.
698
699 Cazorla, M., G. Wolfe, S. Bailey, A. Swanson, H. Arkinson, and T. Hanisco (2015), A new
700 airborne laser-induced fluorescence instrument for in situ detection of formaldehyde throughout
701 the troposphere and lower stratosphere, *Atmospheric Measurement Techniques*, *8*(2), 541-552.

Clairotte, M., T. Adam, A. Zardini, U. Manfredi, G. Martini, A. Krasenbrink, A. Vicet, E. Tournié, and C. Astorga (2013), Effects of low temperature on the cold start gaseous emissions from light duty vehicles fuelled by ethanol-blended gasoline, *Applied Energy*, *102*, 44-54.

Cowling, E. B., C. Furiness, B. Dimitriades, and D. Parrish (2007), Final rapid science synthesis report: Findings from the second Texas air quality study (TexAQS II), *TCEQ contract*(582-4), 65614.

Czader, B. H., D. W. Byun, S.-T. Kim, and W. P. Carter (2008), A study of VOC reactivity in the Houston-Galveston air mixture utilizing an extended version of SAPRC-99 chemical mechanism, *Atmospheric Environment*, *42*(23), 5733-5742.

Dardiotis, C., G. Fontaras, A. Marotta, G. Martini, and U. Manfredi (2015), Emissions of modern light duty ethanol flex-fuel vehicles over different operating and environmental conditions, *Fuel*, *140*, 531-540.

Day, D., P. Wooldridge, M. Dillon, J. Thornton, and R. Cohen (2002), A thermal dissociation laser-induced fluorescence instrument for in situ detection of NO2, peroxy nitrates, alkyl nitrates, and HNO3, *Journal of Geophysical Research: Atmospheres*, *107*(D6), ACH 4-1-ACH 4-14.

de Blas, M., P. Ibáñez, J. A. García, M. C. Gómez, M. Navazo, L. Alonso, N. Durana, J. Iza, G. Gangoiti, and E. S. de Cámara (2019), Summertime high resolution variability of atmospheric formaldehyde and non-methane volatile organic compounds in a rural background area, *Science of the total environment*, *647*, 862-877.

de Gouw, J., J. Gilman, S. W. Kim, B. Lerner, G. Isaacman-VanWertz, B. McDonald, C. Warneke, W. Kuster, B. Lefer, and S. Griffith (2017a), Chemistry of volatile organic compounds in the Los Angeles basin: Nighttime removal of alkenes and determination of emission ratios, *Journal of Geophysical Research: Atmospheres*, *122*(21), 11,843-811,861.

de Gouw, J., L. J. van de Ven, S. Lourens, B. Kemp, and H. van den Brand (2017b), Effects of dust, formaldehyde and delayed feeding on early postnatal development of broiler chickens, *Research in veterinary science*, *112*, 201-207.

Doane, M., and S. Sarenbo (2014), Exposure of farm laborers and dairy cattle to formaldehyde from footbath use at a dairy farm in New York State, *Science of the total environment*, *487*, 65-71.

Dominutti, P. A., T. Nogueira, A. Borbon, M. de Fatima Andrade, and A. Fornaro (2016), One-year of NMHCs hourly observations in São Paulo megacity: meteorological and traffic emissions effects in a large ethanol burning context, *Atmospheric environment*, *142*, 371-382.

EPA (2015), Technical Support Document: EPA's 2011 National-scale Air Toxics Assessment, edited, Environmental Protection Agency.

747 Fibiger, D. L., E. E. McDuffie, W. P. Dubé, K. C. Aikin, F. D. Lopez-Hilfiker, B. H. Lee, J. R.
748 Green, M. N. Fiddler, J. S. Holloway, and C. Ebben (2018), Wintertime overnight NOx removal
749 in a southeastern United States coal-fired power plant plume: A model for understanding winter
750 NOx processing and its implications, *Journal of Geophysical Research: Atmospheres*, *123*(2),
751 1412-1425.
752 Friedfeld, S., M. Fraser, K. Ensor, S. Tribble, D. Rehle, D. Leleux, and F. Tittel (2002),
753 Statistical analysis of primary and secondary atmospheric formaldehyde, *Atmospheric*
754 *Environment*, *36*(30), 4767-4775.
755
756 Garcia, A., R. Volkamer, L. Molina, M. Molina, J. Samuelson, J. Mellqvist, B. Galle, S.
757 Herndon, and C. Kolb (2006), Separation of emitted and photochemical formaldehyde in Mexico
758 City using a statistical analysis and a new pair of gas-phase tracers, *Atmospheric Chemistry and*
759 *Physics*, *6*(12), 4545-4557.
760
761 Green, J. R., M. N. Fiddler, J. S. Holloway, D. L. Fibiger, E. E. McDuffie, P. Campuzano-Jost, J.
762 C. Schroder, J. L. Jimenez, A. J. Weinheimer, and J. Aquino (2019), Rates of Wintertime
763 Atmospheric SO2 Oxidation based on Aircraft Observations during Clear-Sky Conditions over
764 the Eastern United States, *Journal of Geophysical Research: Atmospheres*, *124*(12), 6630-6649.
765
766 Guven, B. B., and E. P. Olaguer (2011), Ambient formaldehyde source attribution in Houston
767 during TexAQS II and TRAMP, *Atmospheric environment*, *45*(25), 4272-4280.
768
769 Hagerman, L. M., V. P. Aneja, and W. A. Lonneman (1997), Characterization of non-methane
770 hydrocarbons in the rural southeast United States, *Atmospheric Environment*, *31*(23), 4017-4038.
771
772 Haskins, J., F. Lopez-Hilfiker, B. Lee, V. Shah, G. Wolfe, J. DiGangi, D. Fibiger, E. McDuffie,
773 P. Veres, and J. Schroder (2019), Anthropogenic control over wintertime oxidation of
774 atmospheric pollutants, *Geophysical Research Letters*, *46*(24), 14826-14835.
775
776 Hassler, B., B. C. McDonald, G. J. Frost, A. Borbon, D. C. Carslaw, K. Civerolo, C. Granier, P.
777 S. Monks, S. Monks, and D. D. Parrish (2016), Analysis of long-term observations of NOx and
778 CO in megacities and application to constraining emissions inventories, *Geophysical Research*
779 *Letters*, *43*(18), 9920-9930.
780
781 He, Y. Ge, J. Tan, K. You, X. Han, J. Wang, Q. You, and A. N. Shah (2009), Comparison of
782 carbonyl compounds emissions from diesel engine fueled with biodiesel and diesel, *Atmospheric*
783 *Environment*, *43*(24), 3657-3661.
784
785 Jaeglé, L., V. Shah, J. Thornton, F. Lopez-Hilfiker, B. Lee, E. McDuffie, D. Fibiger, S. Brown,
786 P. Veres, and T. Sparks (2018), Nitrogen oxides emissions, chemistry, deposition, and export
787 over the Northeast United States during the WINTER aircraft campaign, *Journal of Geophysical*
788 *Research: Atmospheres*, *123*(21), 12,368-312,393.
789
790 Jenkin, M., J. Young, and A. Rickard (2015), The MCM v3. 3.1 degradation scheme for
791 isoprene, *Atmospheric Chemistry and Physics*, *15*(20), 11433.
792

Jenkin, M. E., S. M. Saunders, and M. J. Pilling (1997), The tropospheric degradation of volatile organic compounds: a protocol for mechanism development, *Atmospheric Environment*, *31*(1), 81-104.

Jobson, T., and Y. Huangfu (2016), Impact of cold climates on vehicle emissions: The cold start air toxics pulse*Rep.*, Department of Civil and Environmental Engineering, University of Washington, Pullman, WA.

Knoll, K., B. West, S. Huff, J. Thomas, J. Orban, and C. Cooper (2009), Effects of mid-level ethanol blends on conventional vehicle emissions*Rep. 0148-7191*, SAE Technical Paper.

Koss, A., J. d. Gouw, C. Warneke, J. Gilman, B. Lerner, M. Graus, B. Yuan, P. Edwards, S. Brown, and R. Wild (2015), Photochemical aging of volatile organic compounds associated with oil and natural gas extraction in the Uintah Basin, UT, during a wintertime ozone formation event, *Atmospheric Chemistry and Physics*, *15*(10), 5727-5741.

Kurosu, T. P., K. Chance, X. Liu, R. Volkamer, T.-M. Fu, D. Millet, D. J. Jacob, and P. Levelt (2007), Seasonally resolved global distributions of glyoxal and formaldehyde observed from the Ozone Monitoring Instrument on EOS Aura, *Proc. of Anais XIII Simpósio Brasileiro de Sensoriamento Remoto*, 6461-6464.

Laursen, K. K., D. P. Jorgensen, G. P. Brasseur, S. L. Ustin, and J. R. Huning (2006), HIAPER: The next generation NSF/NCAR research aircraft, *Bulletin of the American Meteorological Society*, *87*(7), 896-909.

Lehto, J., A. Oasmaa, Y. Solantausta, M. Kytö, and D. Chiaramonti (2014), Review of fuel oil quality and combustion of fast pyrolysis bio-oils from lignocellulosic biomass, *Applied Energy*, *116*, 178-190.

Li, C., S. C. Tsay, J. S. Fu, R. R. Dickerson, Q. Ji, S. W. Bell, Y. Gao, W. Zhang, J. Huang, and Z. Li (2010), Anthropogenic air pollution observed near dust source regions in northwestern China during springtime 2008, *Journal of Geophysical Research: Atmospheres*, *115*(D7).

Li, X., T. Brauers, A. Hofzumahaus, K. Lu, Y. Li, M. Shao, T. Wagner, and A. Wahner (2013), MAX-DOAS measurements of NO2, HCHO and CHOCHO at a rural site in Southern China, *Atmospheric Chemistry and Physics*, *13*(4), 2133.

Liang, W., M. Lv, and X. Yang (2016), The effect of humidity on formaldehyde emission parameters of a medium-density fiberboard: Experimental observations and correlations, *Building and Environment*, *101*, 110-115.

Lin, Y. C., J. J. Schwab, K. L. Demerjian, M. S. Bae, W. N. Chen, Y. Sun, Q. Zhang, H. M. Hung, and J. Perry (2012), Summertime formaldehyde observations in New York City: Ambient levels, sources and its contribution to HOx radicals, *Journal of Geophysical Research: Atmospheres*, *117*(D8).

838 Luecken, W. Hutzell, M. Strum, and G. Pouliot (2012), Regional sources of atmospheric
839 formaldehyde and acetaldehyde, and implications for atmospheric modeling, *Atmospheric*
840 *environment*, *47*, 477-490.
841 Luecken, S. Napelenok, M. Strum, R. Scheffe, and S. Phillips (2018), Sensitivity of ambient
842 atmospheric formaldehyde and ozone to precursor species and source types across the United
843 States, *Environmental science & technology*, *52*(8), 4668-4675.
844
845 Marvin, M. R., G. M. Wolfe, R. J. Salawitch, T. P. Canty, S. J. Roberts, K. R. Travis, K. C.
846 Aikin, J. A. de Gouw, M. Graus, and T. F. Hanisco (2017), Impact of evolving isoprene
847 mechanisms on simulated formaldehyde: An inter-comparison supported by in situ observations
848 from SENEX, *Atmospheric Environment*, *164*, 325-336.
849
850 Parrish, D., D. Allen, T. Bates, M. Estes, F. Fehsenfeld, G. Feingold, R. Ferrare, R. Hardesty, J.
851 Meagher, and J. Nielsen-Gammon (2009a), Overview of the second Texas air quality study
852 (TexAQS II) and the Gulf of Mexico atmospheric composition and climate study (GoMACCS),
853 *Journal of Geophysical Research: Atmospheres*, *114*(D7).
854
855 Parrish, D., W. C. Kuster, M. Shao, Y. Yokouchi, Y. Kondo, P. D. Goldan, J. A. de Gouw, M.
856 Koike, and T. Shirai (2009b), Comparison of air pollutant emissions among mega-cities,
857 *Atmospheric Environment*, *43*(40), 6435-6441.
858
859 Parrish, D., T. Ryerson, J. Mellqvist, J. Johansson, A. Fried, D. Richter, J. Walega, R. d.
860 Washenfelder, J. De Gouw, and J. Peischl (2012), Primary and secondary sources of
861 formaldehyde in urban atmospheres: Houston Texas region, *Atmospheric Chemistry and Physics*,
862 *12*(7), 3273-3288.
863
864 Pikelnaya, O., J. H. Flynn, C. Tsai, and J. Stutz (2013), Imaging DOAS detection of primary
865 formaldehyde and sulfur dioxide emissions from petrochemical flares, *Journal of Geophysical*
866 *Research: Atmospheres*, *118*(15), 8716-8728.
867
868 Rappenglück, B., P. Dasgupta, M. Leuchner, Q. Li, and W. Luke (2010), Formaldehyde and its
869 relation to CO, PAN, and SO 2 in the Houston-Galveston airshed, *Atmospheric Chemistry and*
870 *Physics*, *10*(5), 2413-2424.
871
872 Rawlings, J. O., S. G. Pantula, and D. A. Dickey (2001), *Applied regression analysis: a research*
873 *tool*, Springer Science & Business Media.
874
875 Ryerson, T., A. Andrews, W. Angevine, T. Bates, C. Brock, B. Cairns, R. Cohen, O. Cooper, J.
876 De Gouw, and F. Fehsenfeld (2013), The 2010 California research at the Nexus of air quality and
877 climate change (CalNex) field study, *Journal of Geophysical Research: Atmospheres*, *118*(11),
878 5830-5866.
879
880 Salem, and M. Böhm (2013), Understanding of formaldehyde emissions from solid wood: an
881 overview, *BioResources*, *8*(3), 4775-4790.
882

Salmon, O., P. Shepson, X. Ren, H. He, D. Hall, R. Dickerson, B. Stirm, S. Brown, D. Fibiger, and E. McDuffie (2018), Top-down estimates of NOx and CO emissions from Washington, DC-Baltimore during the WINTER campaign, *Journal of Geophysical Research: Atmospheres*, *123*(14), 7705-7724.

Saunders, S. M., M. E. Jenkin, R. Derwent, and M. Pilling (2003), Protocol for the development of the Master Chemical Mechanism, MCM v3 (Part A): tropospheric degradation of non-aromatic volatile organic compounds.

Shah, V., L. Jaeglé, J. A. Thornton, F. D. Lopez-Hilfiker, B. H. Lee, J. C. Schroder, P. Campuzano-Jost, J. L. Jimenez, H. Guo, and A. P. Sullivan (2018), Chemical feedbacks weaken the wintertime response of particulate sulfate and nitrate to emissions reductions over the eastern United States, *Proceedings of the National Academy of Sciences*, *115*(32), 8110-8115.

Sparks, T. L., C. J. Ebben, P. J. Wooldridge, F. D. Lopez-Hilfiker, B. H. Lee, J. A. Thornton, E. E. McDuffie, D. L. Fibiger, S. S. Brown, and D. D. Montzka (2019), Comparison of Airborne Reactive Nitrogen Measurements During WINTER, *Journal of Geophysical Research: Atmospheres*, *124*(19), 10483-10502.

Timonen, H., P. Karjalainen, E. Saukko, S. Saarikoski, P. Aakko-Saksa, P. Simonen, T. Murtonen, M. Dal Maso, H. Kuuluvainen, and M. Bloss (2017), Influence of fuel ethanol content on primary emissions and secondary aerosol formation potential for a modern flex-fuel gasoline vehicle, *Atmospheric Chemistry and Physics*, *17*(8), 5311.

VanderSchelden, G., B. de Foy, C. Herring, S. Kaspari, T. VanReken, and B. Jobson (2017), Contributions of wood smoke and vehicle emissions to ambient concentrations of volatile organic compounds and particulate matter during the Yakima wintertime nitrate study, *Journal of Geophysical Research: Atmospheres*, *122*(3), 1871-1883.

Warneke, C., S. McKeen, J. De Gouw, P. Goldan, W. Kuster, J. Holloway, E. Williams, B. Lerner, D. Parrish, and M. Trainer (2007), Determination of urban volatile organic compound emission ratios and comparison with an emissions database, *Journal of Geophysical Research: Atmospheres*, *112*(D10).

Warneke, C., M. Trainer, J. A. de Gouw, D. D. Parrish, D. W. Fahey, A. Ravishankara, A. M. Middlebrook, C. A. Brock, J. M. Roberts, and S. S. Brown (2016), Instrumentation and measurement strategy for the NOAA SENEX aircraft campaign as part of the Southeast Atmosphere Study 2013, *Atmospheric measurement techniques*, *9*(7), 3063.

Weinheimer, A., J. Walega, B. Ridley, B. Gary, D. Blake, N. Blake, F. Rowland, G. Sachse, B. Anderson, and J. Collins (1994), Meridional distributions of NOx, NOy, and other species in the lower stratosphere and upper troposphere during AASE II, *Geophysical research letters*, *21*(23), 2583-2586.

White, D., S. Gurung, D. Zhao, Y. Farnell, J. Byrd, S. McKenzie, D. Styles, and M. Farnell (2018), Evaluation of layer cage cleaning and disinfection regimens, *Journal of Applied Poultry Research*, *27*(2), 180-187.

Wild, R. J., P. M. Edwards, W. P. Dubé, K. Baumann, E. S. Edgerton, P. K. Quinn, J. M. Roberts, A. W. Rollins, P. R. Veres, and C. Warneke (2014), A Measurement of Total Reactive Nitrogen, NO y, together with NO2, NO, and O3 via Cavity Ring-down Spectroscopy, *Environmental science & technology*, *48*(16), 9609-9615.

Wolfe, M. R. Marvin, S. J. Roberts, K. R. Travis, and J. Liao (2016), The framework for 0-D atmospheric modeling (F0AM) v3. 1, *Geoscientific Model Development*, *9*(9), 3309-3319.

Yrieix, C., A. Dulaurent, C. Laffargue, F. Maupetit, T. Pacary, and E. Uhde (2010), Characterization of VOC and formaldehyde emissions from a wood based panel: Results from an inter-laboratory comparison, *Chemosphere*, *79*(4), 414-419.

Yuan, B., L. Kaser, T. Karl, M. Graus, J. Peischl, T. L. Campos, S. Shertz, E. C. Apel, R. S. Hornbrook, and A. Hills (2015), Airborne flux measurements of methane and volatile organic compounds over the Haynesville and Marcellus shale gas production regions, *Journal of Geophysical Research: Atmospheres*, *120*(12), 6271-6289.

Zhang, H., J. Li, Q. Ying, B. B. Guven, and E. P. Olaguer (2013), Source apportionment of formaldehyde during TexAQS 2006 using a source-oriented chemical transport model, *Journal of Geophysical Research: Atmospheres*, *118*(3), 1525-1535.

Zhu, L., D. J. Jacob, F. N. Keutsch, L. J. Mickley, R. Scheffe, M. Strum, G. González Abad, K. Chance, K. Yang, and B. Rappenglück (2017), Formaldehyde (HCHO) as a hazardous air pollutant: Mapping surface air concentrations from satellite and inferring cancer risks in the United States, *Environmental science & technology*, *51*(10), 5650-5657.